Emergent vascular network inhomogeneities and resulting blood flow patterns in a growing tumor

M. Welter[a], K. Bartha[b], H. Rieger[a],*

[a]*Theoretische Physik, Universität des Saarlandes, PF 151150, 66041 Saarbrücken, Germany*
[b]*Department of Medical Biochemistry, Semmelweis University, Budapest, Hungary*

Abstract

Tumors acquire sufficient oxygen and nutrient supply by coopting host vessels and neovasculature created via angiogenesis, thereby transforming a highly ordered network into chaotic heterogeneous tumor specific vasculature. Vessel regression inside the tumor leads to large regions of necrotic tissue interspersed with isolated surviving vessels. We extend our recently introduced model to incorporate Fahraeus–Lindqvist- and phase separation effects, refined tissue oxygen level computation and drug flow computations. We find, unexpectedly, that collapse and regression accelerates rather than diminishes the perfusion and that a tracer substance flowing through the remodeled network reaches all parts of the tumor vasculature very well. The reason for decreased drug delivery well known in tumors should therefore be different from collapse and vessel regression. Implications for drug delivery in real tumors are discussed.
© 2007 Elsevier Ltd. All rights reserved.

Keywords: Cancer; Angiogenesis modeling; Blood flow heterogeneities; Remodeling of vessel networks; Drug flow simulations

1. Introduction

A malignant tumor, cancer, remodels actively the blood vessel network of normal tissue into a characteristic tumor vasculature (Holash et al., 1999a, b): A well perfused region of the network at the tumor periphery provides sufficient oxygen and nutrient for further tumor growth, whereas an extremely sparse network with a low vascular density in the tumor center produces a necrotic core. The process leading to a high vascular density at the outer rim is known as angiogenesis, the production of new vessels from old ones via the stimulus of tumor secreted growth factors (Carmeliet and Jain, 2000). The regression of vessels inside the tumor is related to unstable vessel morphology and abnormal blood flow dynamics as well as increased solid stress generated by the tumor—for a discussion see Bartha and Rieger (2006). The emerging vascular tumor network is thus extremely inhomogeneous and has geometric, in particular fractal, properties that are very different from normal vasculature (Baish and Jain, 2000). As a consequence also blood flow patterns inside this network are highly irregular and might have an impact upon drug delivery (Minchinton and Tannock, 2006).

This paper is concerned with a mathematical model for a situation sketched above. There is already a large amount of work on the mathematical modeling of tumor-induced angiogenesis (for reviews see, e.g., Mantzaris et al., 2004; Preziosi, 2003) and can roughly be classified into two groups: The first group concentrates on blood vessel densities rather than vessel morphology, as in continuum partial differential equation (Byrne and Chaplain, 1995; Levine et al., 2001) or in locally coupled map lattice (Sansone et al., 2001) approaches. Todays most sophisticated models (Breward et al., 2003), so-called multi-phase models even track density profiles of different tissue types. Mechanical interaction is included in terms of constitutive laws. Hence, also the effect of solid pressure on cells can be respected. The current research situation is reviewed in (Byrne et al., 2006). Due to the absence of individual blood "vessels" these models do not contain neither the information on the geometrical and morphological properties of the vascular network nor on hydrodynamic blood flow characteristics.

---

*Corresponding author. Tel.: +49 681 302 3969; fax: +49 681 302 4899.
E-mail address: h.rieger@mx.uni-saarland.de (H. Rieger).

The second group of works represents vessels as interconnected lattice patterns, line segments, or continuous curves. As a crucial simplification either a static tumor is assumed (Anderson and Chaplain, 1998; McDougall et al., 2002; Tong and Yuan, 2001; Sun et al., 2005), or a proliferating tumor is considered in a static network topology. An example for the latter is the work of (Alarcon et al., 2003), where a cellular automaton model was introduced in which automaton elements, are identified with vessels, extracellular matrix (ECM), tumor cells (TCs) or normal cells. TCs and normal cells can proliferate or die according to the O_2 level and other factors, creating a competition between TCs and normal cells. The vessel network is initialized to a hexagonal grid and remains static. The O_2 concentration is computed by a standard diffusion equation with vessel sites as sources and other tissues as consumers. Based on this the invasiveness of TCs under different O_2 conditions is studied. This work has been progressively extended into a complex multi-scale model (Betteridge et al., 2006) which includes an improved model for dynamic vessel radius adaption in response to various stimuli (Pries et al., 1998), "pressure" effects i.e. competition for space, a vascular endothelial growth factor (VEGF) concentration field, implemented in analogy to O_2, biochemical details, including cell cycles and factors related to proliferation and apoptosis, modeled via ordinary differential equations. Despite these improvements the basic limitation of a topologically static vessel network remains and for many tumor types the applicability of this model is restricted to the first few days of the existence of the tumor.

A paradigmatic angiogenesis model with a static tumor (Anderson and Chaplain, 1998) describes actually the experimental situation in the so-called "rabbit eye model" (Gimbrone et al., 1974), in which a small growth factor (or TAF, i.e. tumor angiogenic factor) source is implanted in the cornea of the eye. Stimulated by TAF, angiogenesis occurs, whereupon multiple sprouts migrate toward the tumor. Excessive branching and loop formation happens close to the tumor, culminating in an extremely dense network. Since the cornea is initially free of normal vessels this situation can also be denoted as "pure vessel-ingrowth". The continuous theoretical model of (Anderson and Chaplain, 1998) includes three fields for: endothelial cell (EC) density, fibronectin, a component of the ECM also secreted by ECs; TAF concentration. The TAF field is initialized once with a decreasing profile from the tumor to the parent vessel. Later on, TAF is locally consumed by ECs. Fibronectin is produced and consumed locally by ECs and does not diffuse. EC fluxes are driven by a random motility (diffusion), chemotaxis via GF gradients, and haptotaxis via fibronectin gradients (gradients of adhesion). The discretized version uses probabilities (derived from discretized diffusion equations with source and sink terms) for biased random walks of individual ECs at sprouting tips. These tip ECs leave a path occupied with trailing ECs, which can randomly initiate further sprouts if

TAF concentration is high enough. The basic model has received considerable upgrades; see (Chaplain et al., 2006) for a review. The most recent version (McDougall et al., 2006) includes blood flow rate computations and the sophisticated dynamic vessel radius adaptation procedure (Pries et al., 1998) as used in (Betteridge et al., 2006), making it feasible to study drug delivery by simulations of a tracer substance flowing through the vasculature. A shortcoming that needs to be addressed is that vessels do not penetrate the tumor. In the latest studies (with the most realistic network), the tumor is actually not explicitly represented, instead the lower boundary of the simulated domain is identified with the invasive edge. Hence drug uptake by the tumor varies by three orders of magnitude, depending on whether a thick vessels is near the boundary or not.

This general concept has been adopted in third group of tumor simulators for modeling pure vessel in-growth into a non-static tumor, neglecting existing host vessels. For instance Zheng et al. (2005), designed a hybrid tumor simulator to study highly invasive tumor types like glioma brain cancers. There, an extensive framework is developed, where the tumor is treated as viscous fluid and the topology of the sharp tissue-tumor interface is described by sophisticated level-set techniques. The discrete part involves the angiogenesis model by Anderson and Chaplain (1998), where the generated capillary network serves as additional source for nutrients and influences the evolution of the tumor considerably. In recent work Lowengrub et al. (2007) presented a glioma model where temporal and spatial development of cell densities as well as nutrients is described by convection–reaction–diffusion equations also including mechanical properties like intercellular adhesion forces. For angiogenesis a discrete lattice free variant has been adopted (Plank and Sleeman, 2003, 2004).

Here we also want to go beyond the "static network" and the "static tumor" models and combine a dynamically evolving network in the presence of a dynamically changing tumor. Most relevant for our work is the cellular automaton model that was introduced recently by two of us (Bartha and Rieger, 2006) for a two-dimensional and later for a three-dimensional set-up (Lee et al., 2006), designed to reproduce experimental results for solid human melanoma type tumors (Döme et al., 2002, 2007). There it was found that in cutaneous melanoma during tumor growth, there are no signs of directed vessel ingrowth; instead, these tumors appear to grow by co-opting the massive vascular plexus present in the peritumoral connective tissue. The intention in Bartha and Rieger (2006) was to clarify the basic mechanisms leading to the abnormal tumor vasculature, and discuss the implications for assessment of tumor growth. In the model TCs and ECs occupy sites on a regular lattice. ECs form a vessel network circulated by blood. Tumor and vessels interact via O_2 and GF diffusion fields. The temporal evolution of the system is governed by stochastic rules for certain events like TC death, proliferation, sprout formation or vessel collapse.

It turned out that these comparably simple rules and little numerical effort are sufficient to explain many important aspects of tumor vessel morphology.

In this paper we modify and extend this model and incorporate the details taken into account by Alarcon et al. (2003) for static network topologies as described above, and discuss their relevance for the tumor vessel morphology. Then we analyze on the basis of our model how a drug injected into the blood stream distributes over time within the tumor vasculature and compare the results with those for a pure vessel ingrowth-model (McDougall et al., 2006).

The paper is organized as follows: In Section 2 we describe our model. In Section 3 we present the results of the model which can be compared to experimental data, discuss the effect of parameter variations and the relevance of various model details for the global model behavior. In Section 4 we describe how drug flow is modeled and present results of the simulation of an injection of a tracer substance into one part of the vasculature. Section 5 summarizes our results and provides an outlook to further research.

2. The model

The following model definition is conceptually similar to Bartha and Rieger (2006) but implements higher level of detail in the modeling of physiology.

2.1. Description of the system state

Basics: Elements are managed on a regular two dimensional triangular lattice of $l \times l = n$ sites, i.e. we define the set of sites as

$$L = \left\{ \begin{cases} (\delta(x), & \delta \sin(60°)y) & \text{if } y \text{ even} \\ (\delta(x+\frac{1}{2}), & \delta \sin(60°)y) & \text{else} \end{cases} \middle| x, y \in [0, l) \right\}. \tag{1}$$

Each site can be occupied by a single tumor cell, and each bond by a vessel segment. Unoccupied space is part of the extracellular matrix and/or healthy tissue. Fig. 1 illustrates how TCs and vessels are aligned on the lattice. The lattice constant is $\delta = 10 \, \mu m$, chosen deliberately to be of the order of the typical diameter of TCs and ECs.

Definition of the tumor: The tumor is defined as a set of sites $T = \{x \in L, \text{TC present at } x\}$. This means sites in T are associated with single TCs. For any given site $x \in T$ it is assumed that the space occupied by the cells corresponds roughly to the Voronoi region around x, i.e. the points in space that are closer to x than any other site. The hexagon shown in Fig. 1 is exactly such a Voronoi region and indicates a TC. During the growth of the tumor necrotic regions will arise. At the time t, we refer to these by the set of sites T_{necro} where a TC was removed at some time in the past $t' < t$, excluding the current set of tumor cells: $T_{necro} = \bigcup_{t' < t} T(t') \backslash T(t)$. To determine whether a site x is inside the tumor we use a polar map $x_T(\theta)$ which tracks
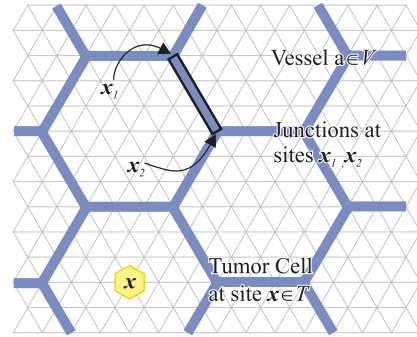

Fig. 1. Illustration of vessels and TCs. A tumor cell (TC) is indicated as yellow hexagon. TCs are centered at lattice sites. Sites always represent single cells. Thereby the diameter of the cells is of the order of the lattice constant. Vessels are indicated as blue bars. In contrast to TCs, they are associated with the bonds of the lattice, thereby constraining their orientation to the main lattice directions. A single vessel $a = (i, j)$ is highlighted by a black outline. This vessel spans between sites labeled x_i and x_j. Vessel may span multiple sites like those that are indicated here. The initial networks for the studies in Section 3.2 consists of a hexagonal pattern. The hexagonal vessel arrangement here would represent a tiny part of such a network. Note that the tumor grows in it's own layer unhampered by vessel. Interactions are predominantly mediated by growth factor and oxygen fields, although information about the spatial coverage also plays an important role.

the extend of the tumor in radial direction, where θ is the polar angle measured relative to the center of the tumor.

Definition of the micro-vascular system: The micro-vascular system evolves in a separate layer, i.e. vessel elements can pass sites where TCs are also present. From the theoretical point of view the vessel network is a graph where the edges represent vessel segments with associated hemodynamic and geometry properties. Hence, the topology is described by the graph $G = (N, V)$, where $V = \{(i, j), i, j \in N\}$ is the set of vessel segments, i, j denote attached junction nodes in N. We denote the position of a node i with $x_i \in L$. Analogously we refer to various properties of vessels, nodes or TCs via sub-scripts, i.e q_a for the flow-rate in some vessel a.

In our current implementation vessels are allowed to span multiple bonds/sites. For convenience $x \in a$ denotes a site that is covered by a vessel $a \in V$, including the endpoints x_i, x_j. For each vessel in the set of potentially perfused vessels $V_{circ} \subset V$ it is required that least two disjoint paths to the system boundaries must exist.

Blood flow modeling: Blood flow for vessels in V_{circ} is modeled as laminar steady flow through ideal pipes of radius r and length l. Therefore Hagen–Poiseuille's Law is applicable to compute flow rate q and wall shear stress f from the blood pressure difference of the endpoints $p_i - p_j$:

$$q = \frac{\pi}{8} \cdot \frac{r^4}{\eta} \cdot \left(\frac{p_i - p_j}{l} \right), \tag{2}$$

$$f = \frac{r}{2} \cdot \left(\frac{p_i - p_j}{l} \right). \tag{3}$$

To account for the fact that blood is a non-Newtonian fluid with complex flow behavior, it is common to introduce an effective viscosity $\eta = \eta_0 \cdot \eta_{rel}(H, r)$ depending on local

vessel radius r and hematocrit H (red blood cell volume fraction). In simulations which incorporate this effect, we base our calculations on the formula in Pries et al. (1994). It is derived from in vivo data and is used in various other works (Ji et al., 2006; Alarcon et al., 2003; McDougall et al., 2006). Since the definition of η_{rel} is rather lengthy we refer to Fig. 8 and to the original work of Pries et al.

In blood vessel networks the distribution of hematocrit is usually not homogeneous, instead RBCs tend to enter the branch with faster flow—known as phase-separation or plasma-skimming effect (Fung, 1993). To calculate the hematocrit we rely again on an empirical formula. Pries et al. (1990) found a "bifurcation law":

$$QH_b = g(QH_a, r_a, r_b, r_c, q_a, q_b, q_c), \qquad (4)$$

which relates the RBC flow $QH_b = q_b H_b$ in a branch b to the RBC flow QH_a in a parent vessel a in dependence on the radii and the flow rates of all three vessels a, b, c at the bifurcation.

For the definition of the function g we refer again to the original work. Note that the relation is valid only for arterial bifurcation. The case where two or more branches merge into a larger one is trivial for obvious reasons. Furthermore g is symmetric in b and c such that RBC mass is conserved $QH_b + QH_c = QH_a$. During the simulation it is ensured that no more that three vessels meet at some node.

To compute the global hematocrit distribution when the blood flow rates are known, vessels must be processed in consecutive order such that the upstream hematocrit has already been determined when a downstream child is processed. That is because via (4) the hematocrit in a given vessel depends on the hematocrit of all vessels stream upwards. The hematocrit H_0 at the uppermost in-flow vessels is fixed as a boundary condition. Graph-theoretically this problem of traversal order is known as finding a topological sorting and standard algorithms can be applied (Cormen et al., 1990).

Furthermore mass preservation dictates that the sum of inflow and outflow equals zero for each node $i \in N$ (Kirchhoff's Law):

$$0 = \sum_{j \in Nb(i)} q_{ij} = \sum_{j \in Nb(i)} S_{ij} \cdot (p_i - p_j), \qquad (5)$$

where $Nb(i)$ are adjacent nodes of i in the network. To find the flow and pressure distribution when the flow conductivities S_{ij}—and therefore hematocrits—are known, the system of linear equations in the nodal pressures (5) must be solved with appropriate boundary conditions.

Together (2), (5) and the hematocrit computation procedure form a complex system of non-linear equations where it is impossible to solve for flow and hematocrit simultaneously. Hence an iterative approach was suggested in the literature Pries et al. (1990) which is commonly used now (Ji et al., 2006; Alarcon et al., 2003): First an initial guess for the hematocrit is chosen. Until convergence, flow and hematocrit are updated successively assuming constant

hematocrit and constant flow respectively. To solve the pressure–potential equations we use a modern sparse LU factorization library (Davis, 2004) which can efficiently handle large systems with 10,000 of variables. The naive outer fix-point iteration however resulted in poor convergence due to over-and- undershooting. Therefore we employ a dampened iteration which has the same fix-points:

$$\mathbf{q}_{i+1} = \mathbf{q}(\mathbf{H}_i),$$
$$\mathbf{H}_{i+1} = \mathbf{H}_i \cdot 2/3 + 1/3 \cdot \mathbf{H}(\mathbf{q}_{i+1}), \qquad (6)$$

with the stopping condition $\|\mathbf{H}_{i+1} - \mathbf{H}_i\|_2 < 10^{-3}$, where i is the iteration number while $\mathbf{H}$ and $\mathbf{q}$ denote vectors which contain data values from the individual vessel segments. We choose dirichlet type boundary-conditions, where the pressure in boundary nodes is prescribed and decreases from $p^{(max)}$ at $(0,0)$ to $(p^{(max)} + p^{(min)})/2$ at $(0,l)$ and $(l,0)$ further to $p^{(min)}$ at (l,l).

Definition of the oxygen field: The tumor and the vascular system interact via oxygen and growth factor fields. Our unit-less oxygen field c_o is given by the solution of the stationary diffusion-equation:

$$\Delta c_o - \kappa c_o + \alpha(c_o^{(B)} - c_o) = 0, \qquad (7)$$

with the consumption-rate coefficient κ, the source coefficient α, and the blood oxygen level $c_o^{(B)}$. We update the O_2 field by finding the stationary state because the O_2 diffusion constant is of the order of 2.4×10^{-5} cm^2/s which means that the relaxation time after a configuration change is negligible compared to cell proliferation rates, which is of the order of an hour.

For simplicity and efficiency we define a linear O_2-uptake $-\kappa c_o$, as approximation to a more realistic non-linear Michaelis–Menten type relationship (i.e. $-Ac_o/[B + c_o]$). At least within, or close to the tumor the saturation regime of a MM-uptake would be irrelevant, since tumor cells usually suffer from hypoxia. Furthermore κ varies with the tissue type: it is set to $\kappa^{(T)}$ for $\mathbf{x} \in T$ (tumor), 0 for $\mathbf{x} \in T_{necro}$ (necrotic tumor) and $\kappa^{(M)}$ otherwise (ECM/normal tissue). The O_2 transport through the vessels wall is predominantly a diffusion process driven by the PO$_2$ difference between blood ($c_o^{(B)}$) and tissue (c_o) at the vessel wall. Therefore it is common to model the oxygen release as the source term $\alpha(c_o^{(B)} - c_o)$. In the context of our continuum description the coefficient α has the meaning of O_2 amount released per time per volume element, which implicitly includes parameters like wall permeability and circumference. For simplicity we treat all vessels equal i.e. $\alpha(\mathbf{x}) = \alpha^{(0)}$ at vessel occupied sites $\mathbf{x} \in a \in V_{circ}$, where $\alpha^{(0)}$ is a constant. Naturally $\alpha(\mathbf{x}) = 0$ at non-vessel-sites.

For the blood-O_2 level $c_o^{(B)}$, we assume that it is essentially proportional to the blood hematocrit—following (Alarcon et al., 2003)—and neglecting the fact that oxygen leaves the vessel. Considering that the PO$_2$ drops only by about a factor of 2 while blood flows through the

body this is likely not to pose a problem. Performing computations with a sophisticated model as presented by Secomb et al. (2004), would be numerically very hard. Their model includes intravascular O_2 variability, as well as the nonlinear saturation behavior of hemoglobin. In our simple approach however we set $c_o^{(B)}(x) = H_a$ for a given $x \in a \in V_{circ}$. At junctions, the average hematocrit is used. An additional pre-factor is not necessary because (i) it would only scale the field values globally; (ii) c_o is unit-less.

Discretizing the diffusion equation by finite differences for the Laplace operator yields the linear system of equations

$$\left(\frac{2}{\delta^2} + \alpha(x) + \kappa(x)\right)c_o(x)$$
$$- \frac{2}{|Nb(x)|\delta^2}\sum_{x' \in Nb(x)} c_o(x') = \alpha(x)c_o^{(B)}(x), \tag{8}$$

where $Nb(x)$ is the set of neighbor sites. It is solved numerically by a multi-grid V-Cycle with a fixed number of Jacobi iterations at each level (Briggs et al., 2001). Since the sources have only a spatially limited effect, the field does not change much when vessels are added or removed. Hence, the solution from the previous time-step is taken as initial guess. This allows rather efficient updates with a small number of iterations.

Definition of the growth factor field: The modeling of growth factor distribution c_g is also based on a reaction–diffusion equation:

$$0 = \Delta c_g - \tilde{\kappa} c_g + \tilde{\alpha},$$
$$\tilde{\alpha}(x) = \tilde{\alpha}^{(0)} \quad \text{for } x \in T_{uo}, \ 0 \text{ else},$$
$$\tilde{\kappa} = const, \tag{9}$$

where $T_{uo} \subset T$ denotes the set of tumor sites for which $c_o < \theta_o^{(prol)}$. We assume that (i) under-oxygenated TCs produce GF at a constant rate $\tilde{\alpha}^{(0)}$, (ii) free GF is removed with the rate $\tilde{\kappa} c_g$ due to binding and degradation. This simple formulation facilitates the solution following a "Greens-function" approach for the operator $\Delta - \tilde{\kappa}$ by super-positioning contributions of individual TCs:

$$c_g(x) = \sum_{x' \in T_{uo}} \tilde{g}(x - x'), \tag{10}$$

$$\tilde{g} = r \mapsto \max[0, \ 1 - r/R^{(g)}], \tag{11}$$

where $R^{(g)}$ is the GF diffusion radius. For our convenience we use a linearly decaying "Greens-function" instead of the correct exponential decay. The model is not critically dependent on the exact GF profile nor on the value range of c_g and this simplification allows us to tune the distance up to which angiogenesis is triggered intuitively via $R^{(g)}$. $R^{(g)}$ also provides a natural cutoff for the "Greens-function" $\tilde{g}$ so updating the field after removal(addition) of TCs is very efficient because it is sufficient to simply subtract(add) the contribution of the respective cells.

2.2. Description of dynamical processes

The system dynamics are governed by the following procedures which are executed in sequence for each time-step of length $\Delta t = 1h$.

TC proliferation: New TCs are put on empty neighbor sites $x \notin T$ of existing TCs with probability $\Delta t / t_{TC}^{(prol)}$ if the local oxygen level is high enough $c_o(x) > \theta_o^{(prol)}$: $T \leftarrow T \cup \{x\}$. Naturally this restricts proliferation to the outer rim. Experiments (Bru et al., 2003) and simulations (Drasdo and Höhme, 2005) have shown that following an exponential growth, proliferation is indeed confined to a small band behind the invasive edge. The simple model here, reminiscent of the Eden model (Eden, 1961) does not capture all the aspects of tumor growth dynamics. For example cell motility is not included. But we consider this as an acceptable approximation for studying vessel morphology under a growing solid tumor (Fig. 2a).

TC death: TCs are removed with probability $p_{TC}^{(Death)} = 1/2$ if the local O_2 concentration is low enough $c_o < \theta_o^{(death)}$ for longer than $t_{TC}^{(uo)}$: $T \leftarrow T \setminus \{x\}$. Since TCs adapt to low oxygen conditions (Iyer et al., 1998), $\theta_o^{(death)} = \theta_o^{(prol)}/10$ is very small. The survival time under hypoxia actually depends strongly on the cell genotype (Yu et al., 2002), promoting the selection of certain species. However for simplicity $t_{TC}^{(uo)}$ has been given a fixed value (Fig. 2b).

Angiogenesis: While adult vessels are normally quiescent, angiogenesis is induced in close proximity to tumors via increased growth factor levels. Thereby the migration of ECs at the sprouting tip is guided by GF gradients (Gerhardt et al., 2003). Tumors also coopt existing vessels (Paku, 1998) but no explicit modeling is required for this phenomenon because tumor cell proliferation is not occluded by vessels. Incorporation of angiogenesis is split into two subprocesses: sprout initiation and migration. Sprouts are initiated with probability $\Delta t / t_{EC}^{(sprout)}$ at vessel-sites if (i) the location $x \in a \in V$ is outside of the tumor (i.e. no sprouting inside the tumor (Holash et al., 1999a)); (ii) the GF level is above a threshold $c_g(x) > \theta_g^{(prol)}$; (iii) the path length to the next bifurcation is greater than $l^{(spr)}$. At the respective sites segments with $l = \delta$, $r = r^{(init)}$ are appended in the direction of the steepest GF increase (Fig. 2c).

At each sprouting tip one further δ segment is added with probability $\Delta t / t_{EC}^{(migr)}$. If another vessel is located at a neighboring site in front of the tip, the new segment creates a junction to the other vessel, forming a potentially blood circulated loop. Here we assume that the sprout direction remains constant, which is not a severe simplification because due to the two-dimensional setting sprouts usually migrate at most ca. 100 μm until another vessel is hit (the situation is different in three space dimensions). Sprouts have been observed to regress after a certain time of not having formed connections (Nehls et al., 1998). To model this, vessels have an associated countdown s (in analogy to hypoxic TCs) which is incremented each time-step. While $s < s^{(max)}$ vessels are guaranteed not to be removed due to
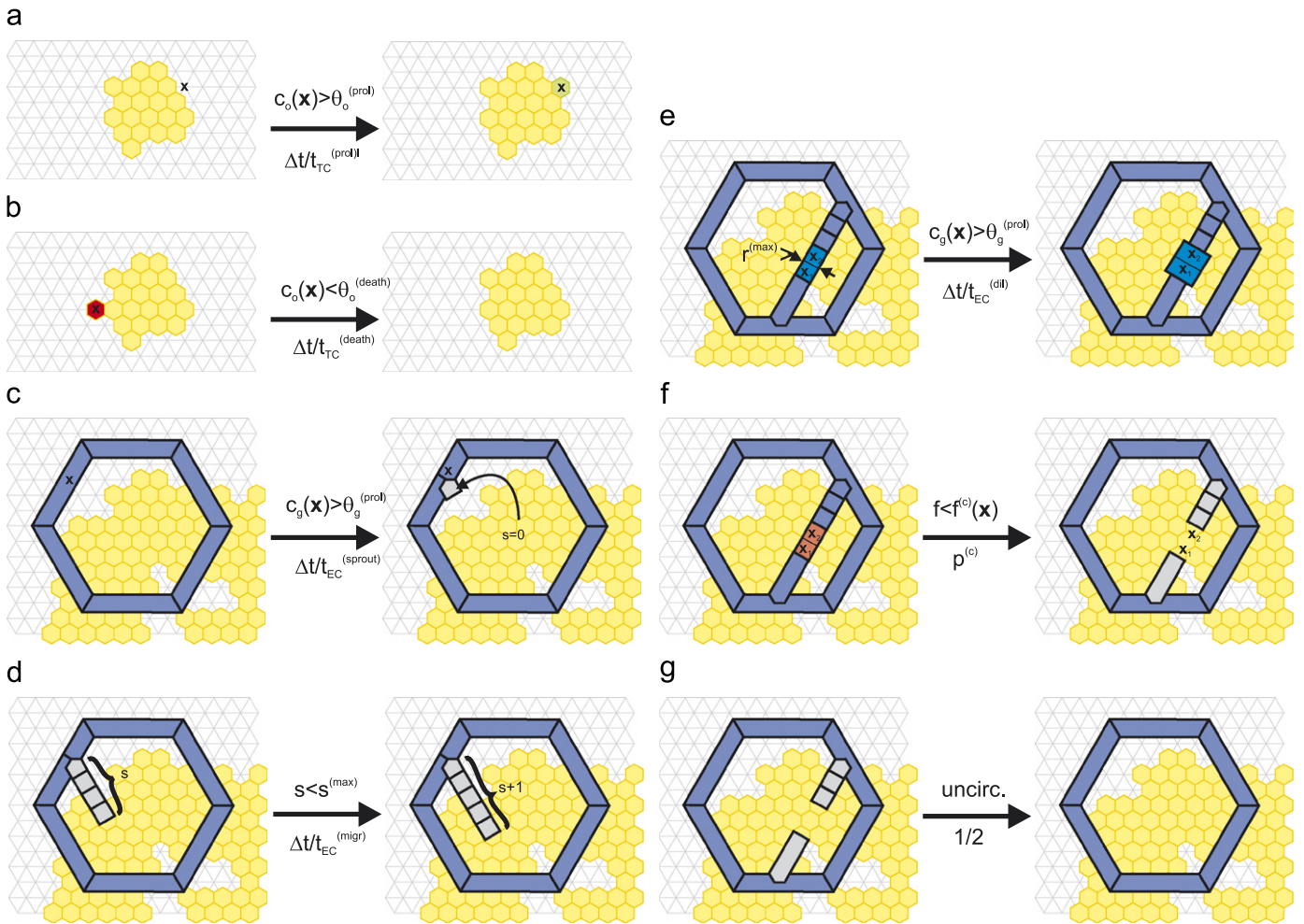
Fig. 2. Illustration of the dynamic processes of the system. Tumor cells are indicated as yellow hexagons. Circulated vessels are indicated as blue bars. Vessels are drawn in gray color if uncirculated. This also includes sprouting tips. The meaning of each subfigure is as follows: (a) Tumor cells proliferate by occupying neighbor sites if $c_o(\mathbf{x}) > \theta_o^{(prol)}$ with a rate $\Delta T / t_{TC}^{(prol)}$; (b) tumor cells die if they have been exposed to low oxygen $c_o(\mathbf{x}) < \theta_o^{(death)}$ for longer than $t_o^{(uo)}$ with a rate $\Delta T / t_{TC}^{(death)}$; (c) sprouts form if $c_g(\mathbf{x}) > \theta_g^{(prol)}$ with rate $\Delta T / t_{EC}^{(sprout)}$; (d) sprouts grow further with by appending segments with rate $\Delta T / t_{EC}^{(migr)}$ until $s > s^{(max)}$; (e) vessels dilate with rate $\Delta T / t_{EC}^{(dil)}$ for each subsegment where $c_g(\mathbf{x}) > \theta_g^{(prol)}$; (f) vessels collapse with rate $p^{(c)}(a, \mathbf{x})$ if for some subsegment $f_a < f^{(c)}(\mathbf{x})$ and (g) Uncirculated network components are eliminated with rate $1/2$.

being uncirculated. During this period vessels can also start new sprouts which inherit s from their parents. Vessels for which $s \geqslant s^{(max)}$ (i.e. normal non-sprouting vessels) regress rapidly if not circulated (Fig. 2d).

Vessel collapse: Long-term reduction of wall shear stress can cause vessel regression. In tumors solid stresses might cause vessel collapses resulting in reduced perfusion and thereby low shear stresses. Also local angiogenesis inhibitors might be involved in EC apoptosis (Dimmeler and Zeiher, 2000). Furthermore dilated tumor vessels, although tortuous and leaky with inadequate support structures, apparently remain stable (Holash et al., 1999b). In the model this behavior is realized as follows: Let $a \in V$ be a vessel then each occupied lattice bond $(k, l) \in a$ causes a to be removed with probability $p^{(c)}(a, (\mathbf{x}_k + \mathbf{x}_l)/2)$. For uncirculated vessels with $s_a \geqslant s^{(max)}$ it is $p^{(c)} = 1/2$. Sprouts are protected from removal, i.e. $p^{(c)} = 0$ for $s_a < s^{(max)}$. For normal circulated vessels $p^{(c)} = p^{(c)}(a, \mathbf{x})$ depending on local system properties as follows: If either shear force or vessel

radius is above a critical threshold $f_a > f^{(c)}(\mathbf{x})$ or $r_a > r^{(stable)}$ then $p^{(c)} = 0$. Thereby we let $f^{(c)}$ vary spatially to account for increased solid stresses in the tumor. Several functional dependencies are studied, but the basic case involves a radial triangular profile g_1, with limited support $2\delta^{(fc)}$ and peak height $f^{(c,max)}$ centered $\delta^{(fc)}$ microns behind the invasive edge:

$$f^{(c)}(\mathbf{x}, a) = f^{(c)}(\mathbf{x} - \mathbf{x}_{center})$$
$$= f^{(c,max)} \cdot g_1(\|\mathbf{x} - \mathbf{x}_{center}\|, \theta),$$

$$g_1 := x, \theta \mapsto \max\left(0, 1 - \frac{|x - x_T(\theta) - \delta^{(fc)}|}{\delta^{(fc)}}\right). \quad (12)$$

This is inspired by Breward et al. (2003) where it is assumed that the replacement of TCs with necrotic material reduces the solid pressure exerted on vessels. If $f_a \leqslant f^{(c)}(\mathbf{x}, a)$ and $r_a \leqslant r^{(stable)}$ and $a \in V_{circ}$ then $p^{(c)} = p^{(c,max)} \cdot g_1(\|\mathbf{x} - \mathbf{x}_{center}\|, \theta) g_2(r_a) > 0$. For the basic case we also tried to

modulate $p^{(c)}$ with a vessel radius dependent linear function g_2 for which $g_2(r^{(stable)}) = 0$ and $g_2(r^{(init)}) = 1$ (Fig. 2f).

Vessel regression: Uncirculated vessels cannot contribute to nutrient delivery and there is no mechanism in the model that would "repair" such vessels. Hence uncirculated vessels $V \setminus V_{circ}$ are simply removed with probability $1/2$ (Fig. 2g).

Vessel dilation: Vascularization and remodeling of the vascular system surrounding the growing tumor is primarily dependent upon angiogenic sprouting as modelled above. Within the tumor the vascularization program switches to circumferential growth of the initial vasculature by proliferation of endothelial cells within the vessel walls (Erber et al., 2006). This we model by a stepwise vessel dilation in the presence of a high enough VEGF concentration. Experimentally it is found that the radius of tumor vessels is limited by a maximum radius $r^{(max)}$ (Döme et al., 2002). Using the polar map x_θ defined above it is decided whether a vessel segment lies within the tumor. If it does vessel dilatation can occur: each bond $(k, l) \in a$ occupied by a vessel a increases the radius of the respective vessel with probability $\Delta t / t_{EC}^{(dil)}$ if $c_g((x_k + x_l)/2) > \theta_o^{(prol)}$ and $r_a < r^{(max)}$. The added value $\delta^2 / 2\pi l_a$ corresponds to the surface area contribution of an additional EC. To account for surface tension, a smoothing effect is generated by dilating the thinnest vessel at junction bonds (Fig. 2e).

3. Results

Following (Bartha and Rieger, 2006), the base case scenario is one for a malignant melanoma, guided by data from Döme et al. (2002). Further parameter variations and simplifications are presented after the base case results.

3.1. Parameters

The size of the lattice is $l = 1000$ in all of the following experiments. With the mentioned bond length $\delta = 10\,\mu m$, this corresponds to a $10 \times 8\,mm^2$ rectangular area of tissue.

Following (Alarcon et al., 2003), we chose a hexagonal pattern as initial network which is physiologically more reasonable than the "Manhattan" or square pattern in (Bartha and Rieger, 2006) since only three vessels meet at junctions. Also not at least because this facilitates the incorporation of the blood phase-separation effect straight forward as described. Fig. 1 depicts a tiny network section, whereas in Fig. 3 half of the domain is visible. We determined the size of the hexagons according to the microvascular density (MVD) of normal skin. Experimentally MVD is measured by counting the number of vessels which cross a thin slice of tissue. Data from Döme et al. (2002) indicate an MVD of ca. 100 vessels per mm^2. This means the average inter vessel distance is ca. $100\,\mu m$. With $60\,\mu m$ edge-length for the hexagons, the vessel–vessel distance through the center of a hexagon lies between 100 and $120\,\mu m$. Furthermore the fraction of vessel occupied

sites is ca. 0.15. The rectangular grid in our previous work yielded the value 0.2.

The initial tumor is generated by placing a single TC in the center of the system and attaching new TCs at randomly chosen surface sites until the tumor contains $|T(t = 0)| = 1000$ cells.

We set the TC proliferation time to $t_{TC}^{(prol)} = 10\,h$, and assume that ECs proliferate four times slower. Hence, sprout generation time is $t_{EC}^{(sprout)} = 40\,h$. The sprout migration time $t_{EC}^{(migr)} = 1\,h$ is motivated by the experimental results of Nehls et al. (1998): Apparently the sprouts extend roughly $200\,\mu m$ per $20\,h$. This matches with the migration rate here, where a $10\,\mu m$ segment is added per hour. The duration for which sprouts remain active $s^{(max)}$ is set to $20\,h$, also in line with these experiments. The minimum distance from a new sprout to existing junctions $l^{(spr)}$, is a crucial parameter as it controls the MVD in the growth region. It is set to $l^{(spr)} = 30\,\mu m$, in order to match MVD data for the peritumoral region in Döme et al. (2002).

The time for dilation $t_{EC}^{(dil)} = 20\,h$ as well as the maximum radius $r^{(max)} = 30\,\mu m$ are estimated from vessel perimeter measurements in that paper. The stable vessel radius is set to $r^{(stable)} = 20\,\mu m$ due to the absence of thin vessels in tumors. The boundary pressures $p^{(max)}$ and $p^{(min)}$ must now generate typical flow and shear stress values for capillaries. In contrast to Bartha and Rieger (2006) the hemodynamics is here based on empirical formulas. $p^{(min)}$ is set to 0 arbitrarily. $p^{(max)}$ is set to $90\,kPa$ such that the shear force in the initial network is within realistic ranges for capillaries: approximately $10\,Pa$ (Gödde and Kurz, 2001).

$(p^{(max)} - p^{(min)})$ gives rise to a gradient in the diagonal of about $\partial P / \partial l \approx \sqrt{2} \times 9\,Pa/\mu m$. Multiplying this by $\cos(45°)$ for a horizontal vessel and multiplying by $\frac{1}{2}r = \frac{5}{2}\,\mu m$ to get the shear force, results in $f \approx 20\,Pa$. The actual value obtained is $<f> = 10\,Pa$, due to the network geometry.

Clearly the pressure values are not realistic, but this has no negative impact on the model because pressures influence the model only indirectly via flow and shear force. The critical shear force $f^{(c,max)}$ is set to $1\,Pa$ and the collapse probability to $p^{(c,max)}$ to 0.01. The collapse probability determines how far the high MVD zone reaches into the tumor. This value is chosen deliberately, because higher values lead to drastic vessel regression just at the invasive edge. Whereas lower values (e.g. <0.005) would be unfeasible because the mean survival time must not be longer than the time to reach the stable radius. Having $p^{(c,max)}$ fixed means that the critical shear force is the prominent factor determining the central MVD. Parameter variations thereof will be presented after the base case results. The support width $\delta^{(fc)} = 1\,mm$ of the collapse region is motivated by results from Breward et al. (2003).

$\alpha^{(0)}$ controls the strength by which c_o scales with increasing MVD. Giving an estimate is difficult due to the quasi two-dimensional layer that is supplied by a network of three dimensional pipes. We factorized $\alpha^{(0)}$ into (i) the volume of a lattice cell $C \cong \delta^2 h$, (ii) the length of a
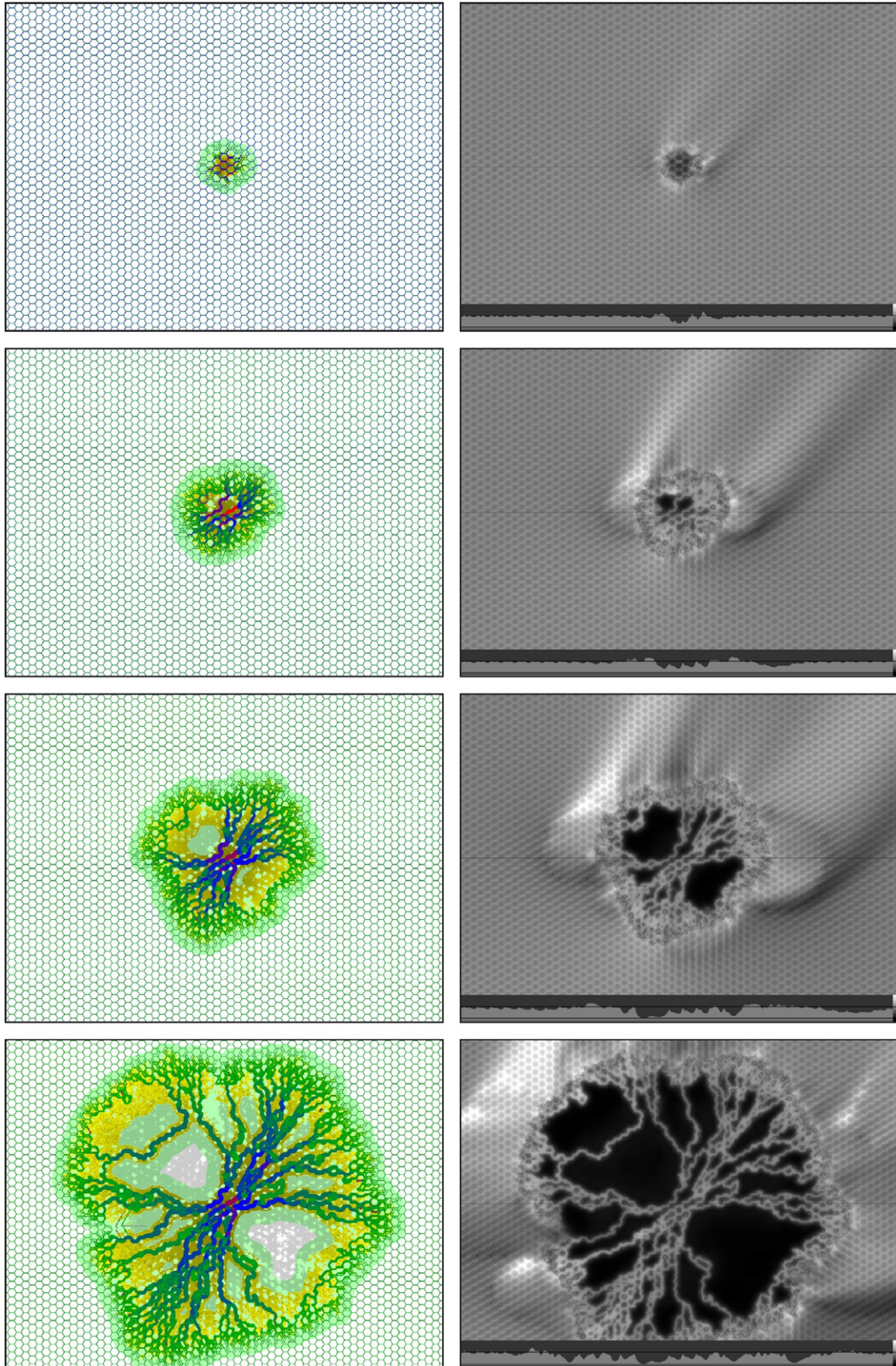
Fig. 3. Left: Tumor and vessel network at $t = 50, 200, 400, 800$. The width of the picture equals 5 mm of tissue. Tumor is yellow, older cells are darker. Vessels are colored coded by flow rate. 0 is green, half the maximum is blue, the global maximum value is red. The global flow goes from the bottom left to the top right. Light green regions indicate GF influence zones. Gray indicated necrotic tissue. Right: Tissue oxygen level: 0.55 is white. The tumor is indicated as thin dark outline. The lower bar shows a cross section profile through the center of the system. The vertical lines indicate the thresholds for proliferation $\theta_o^{(prol)}$ and death $\theta_o^{(death)}$.

vessel subsegment over one lattice-bond $L = \delta$, (iii) the resistance to radial O_2 transport through the vessel wall per axial length $K = 3 \times 10^8$ [cm s mmHg]/mlO$_2$ (Secomb et al., 2004), and (iv) the Krogh diffusion coefficient $D\alpha = 5 \times 10^{-10}$ mlO$_2$/[cm s mmHg]: $\alpha^{(0)} = L/(K C D \alpha)$. The parameter h corresponds to the height of the supplied tissue layer and is deliberately set to 333 μm. Our choice is motivated by two considerations: increasing the MVD should result in noticeable increase in $\langle c_o \rangle$ and the oxygen diffusion range should support 150 μm tissue above and below the vasculature. With parameters as chosen above, we obtain $\alpha^{(0)} = 0.002$. The diffusion radius can be related to the consumption coefficient κ via the Green's function of the operator $[\Delta - \kappa]$ which exhibits asymptotically exponential decay on the length scale $\sqrt{1/\kappa}$. Therefore we set $\kappa^{(M)}$ to $(80 \,\mu\text{m})^{-2}$. The tumor consumption is set to $\kappa^{(T)} = 4\kappa^{(M)}$, i.e. the diffusion radius is halved within the tumor. These parameters yield a mean O_2 concentration of $\langle c_o \rangle = 0.27$ in normal tissue and 0.16 at the tumor center. With the proliferation threshold $\theta_o^{(prol)} = 0.29$ the tumor cannot grow without neovascularization. The threshold for extreme under-oxygenation is set to a value much smaller

than the proliferation threshold: $\theta_o^{(death)} = \theta_o^{(prol)}/10 \ll \langle c_o \rangle$. TCs remain viable under low oxygen conditions for $t_{TC}^{(uo)} = 100$ h. Because the absolute values of the oxygen field are arbitrary, comparisons to experimental data can only be done by observing relative variations.

The growth factor radius is $R^{(g)} = 200$ μm, motivated by the size of the peritumoral region with increased MVD in Döme et al. (2002). The vessel proliferation threshold is very low $\theta_g^{(prol)} = 10^{-4}$, so that essentially all vessels within the full GF radius are affected. In Table 1 all parameter values of the base case scenario are summarized.

3.2. Base-case scenario

System configurations for one representative run at different times are shown in the left column in Fig. 3. The right column shows a map of the oxygen level. Since most TCs are initially under-oxygenized, new vessels emerge within the GF radius in the region around the tumor. Sprouts grow toward the tumor and eventually make contact with other vessels. Once blood flow is established, vessels contribute to the O_2 supply. This leads to increased

Table 1
List of parameters and their symbol together with the values used for the base case scenario

Parameter	Value	Description	Reference
δ	10 μm	Lattice const.	
l	1000	Lattice size	
Δt	1 h	Time step	
$\lvert T(t=0) \rvert$	1000	Initial # TCs	
$\alpha^{(0)}$	0.02	O_2 source coefficient	(Secomb et al., 2004)
$\kappa^{(M)}$	$(80 \,\mu\text{m})^{-2}$	Consumption in normal tissue	(Carmeliet and Jain, 2000)
$\kappa^{(T)}$	$4\kappa^{(M)}$	Consumption tumor tissue	
$\theta_o^{(prol)}$	$0.29 \approx 1.07\langle c_o \rangle$	TC O_2 proliferation threshold	
$\theta_o^{(death)}$	$\theta_o^{(prol)}/10$	TC hypoxia threshold	
$R^{(g)}$	200 μm	Growthfactor diffusion radius	(Döme et al., 2002)
$\theta_g^{(prol)}$	10^{-4}	Sprouting GF threshold	
$H^{(0)}$	0.45	Initial hematocrit	(Pries et al., 1990)
$\eta^{(plasma)}$	4.0×10^{-6} kPa s	Plasma viscosity	(Pries et al., 1990)
$p^{(min)}, p^{(max)}$	0, 90 kPa	Boundary pressure	
$t_{TC}^{(uo)}$	100 h	TC survival time under hypoxia	(Yu et al., 2002)
$t_{TC}^{(prol)}$	10 h	TC proliferation time	
$t_{EC}^{(sprout)}$	40 h	Sprout generation time	
$t_{EC}^{(dil)}$	20 h	Vasodilation time	(Döme et al., 2002)
$t_{EC}^{(migr)}$	1 h	Sprout extension time	(Nehls et al., 1998)
$r^{(init)}$	5 μm	Initial vessel radius	
$r^{(stable)}$	20 μm	Stable vessel radius	(Döme et al., 2002)
$r^{(max)}$	30 μm	Max vessel radius	(Döme et al., 2002)
$s^{(max)}$	20 h	Sprout extension limit	(Nehls et al., 1998)
$l^{(spr)}$	30 μm	Inter-sprout-site distance	(Döme et al., 2002)
$f^{(c,max)}$	0.5 Pa	Peak critical shear force	
$p^{(c,max)}$	0.01	Peak collapse probability	

For the cases in which experimental data are available a reference is given. The other cases are based on educated guesses and the sensibility of the model with respect to variations of these values was studied.

O$_2$ levels, indicated by a small bright band surrounding the low oxygen region. Simultaneously the radius of the central vessels increases. This initial remodeling creates a disturbance in the almost homogeneous global flow also causing long range O$_2$-field variations due to the coupling via the hematocrit. Apparently the O$_2$/hematocrit increase dominates regions close to the central diagonal axis where most blood enters/leaves the tumor. Thereby asymmetrical growth is induced showing that despite neovascularization O$_2$ supply is the limiting factor for TC proliferation. When the tumor grows over the highly vascularized region, vessels begin to collapse. Vessels in the vicinity of tumor cells are continuously exposed to growth factors and thus increase their radius up to $r^{(max)}$. In regions void of vessels, tumor cells die after $t_{TC}^{(uo)}$, due to the lack of oxygen. As expected ca. 100 μm wide cuff remain alive around few surviving vessels.

Despite the star like structure of the network, which is clearly an artifact of the unrealistic flow boundary conditions, we can reproduce general tumor-network features in agreement with the rest of the literature (Holash et al., 1999a, b; Bartha and Rieger, 2006; Döme et al., 2002). Fig. 4 gives a quantitative analysis of the dynamical evolution. The curves are averaged over 20 runs, with different random number generator seeds but otherwise identical parameters. Statistical fluctuations are of the order of 10%, growing toward the tumor center. Fig. 4(f) shows how the tumor density varies with distance r to the center of the system. The tumor periphery moves outward linearly with a speed of 2 μm/h $= 2\Delta r/t_{TC}^{(prol)}$. The factor 2 is typical for Eden growth (Eden, 1961). Fig. 4(a) shows the average microvascular radius (MVR). Since tumor vessels are always enclosed by TCs that produce GF, the radius grows everywhere inside the tumor at a constant rate. At a fixed location this means that as soon as the tumor as grown over it, the radius increases linearly until the threshold $r^{(max)}$ is reached. Hence a plateau is observed when the spatial variations at a fixed time are considered. Fig. 4(b) shows the MVD and agrees with the pictures in Fig. 3 regarding the compartmentalization of the system. There is a region of high MVD which coincides with the TC density drop. Inside the tumor, the MVD drops to 1/4 of the original MVD, since only few vessels survive the collapse process. In Fig. 4(d) it can be seen that the wall shear stress drops by almost two orders of magnitude, even below the critical collapse force $f^{(c,max)} = 1$ Pa. Considering that the support of the band where vessels collapse due to solid pressure is $\delta^{(fc)} = 1$ mm broad, this means that vessels collapse in a narrow shell in the tumor periphery. Hence, altering the rules for the collapse process, leads to different MVDs and network structures as evident in Section 3.4. The drastic reduction in shear stress stems from equally drastic reduction in pressure gradients. In contrast to flow and shear stress, the pressure gradients assume near constant values after the drop at the tumor boundary. Hence, near the tumor center, the vessel radius dependence which is $r(v)^4$ and $r(v)$ for the blood flow rate and shear stress, respectively is responsible for variations of the latter

properties. Fig. 4(e) shows the radial oxygen variations, which are strongly correlated to the MVD variations. Naturally the O$_2$ level drops in the tumor center. The average value in the tissue is $\langle c_o \rangle = 0.275$. In the highly vascularized zone it increases by 30%. In contrast to our previous work the O$_2$ increase is not proportional to the MVD due to the O$_2$ dependent source strength.

Quantitatively our results agree well with the morphological data provided in Döme et al. (2002). They analyzed human malignant melanoma spatially divided into three regions: (i) the tumor center, (ii) the tumor periphery—a 100 μm wide band of tumor immediately adjacent to the invasive edge, and (iii) the peritumoral host tissue—a 200 μm wide band of host tissue immediately adjacent to the periphery. It was found that for tumors larger than 1.5 mm the MVD in (i) drops to 25% of the MVD in normal skin. In (iii) the MVD reaches values up to two times the normal MVD. In terms of radii, the MVR grows from ≈ 8 to $\approx 30-35$ μm in the center, at day 15, and remains constant. From day 12 on the MVR in (ii) and (iii) also remains constant, and grows from (iii) to (ii) to (i).

Boxcounting analysis: The concept of a fractal dimension is often used to characterize differences between normal vasculature and tumor vasculature (Baish and Jain, 2000). One commonly used method to estimate fractal dimension is box-counting, which is carried out by superimposing a grid with box diameter l on the fractal object and counting the number of boxes n which overlap the object. The self similar nature of true fractal object leads to a power law relationship between box count and box size with the fractal dimension d_f as exponent:

$$n(l) \propto l^{-d_f}. \tag{13}$$

d_f is usually extracted by a linear fit in a log–log plot. However in experiments one can usually only measure l over two orders of magnitude. Furthermore natural objects (or rather photographs thereof) are usually not perfectly fractal i.e. box-counting plots exhibit non-constant slopes. Therefore even a small constant regime is often considered sufficient to speak of a fractal dimension (or more truthfully named box-counting dimension); see the discussion in Chung and Chung (2001a, b). Therefore what we mean in following with "fractal dimension" is the number that we obtained by the procedure described below and which is analogous to the way in which this number is extracted from the analysis of experimental data (Gazit et al., 1995; Baish and Jain, 2000; Chung and Chung, 2001a, b).

We did box-counting for the tumor as well as for different parts of the vessel network at the time $t = 1000$ h. At this time the diameter of the tumor is ca. 5 mm. Vessels are treated as ideal line segments, and overlapping boxes are visited by a digital differential analyzer algorithm (Glassner, 1994). TC occupied locations were treated as points. Boxes with size L were shifted by $\max\{L/10 \, \mu m, 16\}^2$ different offsets equidistantly distributed in $[0, L]^2$, and the minimum box-count was taken. The fractal dimension is then estimated as average over the
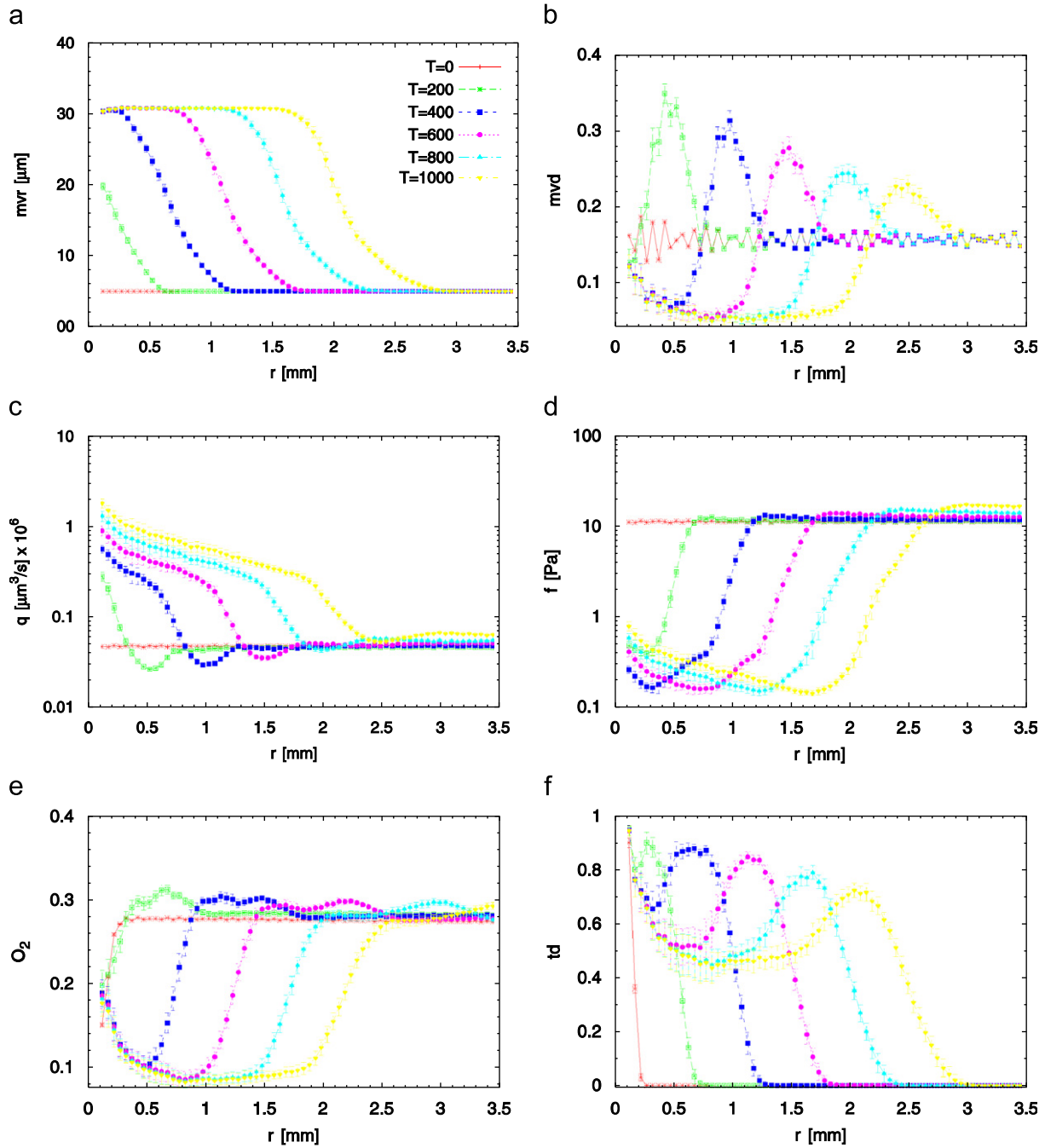
Fig. 4. Various dynamic variables in dependence on the radial distance r to the tumor center: (a) Shows the vessel radius. It decreases with the distance to the tumor, whereas at a fixed distance to the tumor center it increases with time. (b) Shows the microvascular vascular density (MVD) dependence. The MVD is high at the tumor boundary, and low in the tumor center. The maximum value decreases with time due to the asymmetry of the tumor. (c) The flow rate increases by more than an order of magnitude inside the tumor. Whereas (d) shows that the shear force decreases by almost two orders of magnitude. (e) The oxygen level follows roughly the same shape as the MVD. Due to implicitly defined source strengths, the increase in high-MVD regions is much less than simply proportional. (f) Shows the tumor density. One can see that the tumor radius increases linearly in time, as expected according to the eden rule. The density drop eventually becomes less pronounced due to the asymmetric growth.

local slopes of the log–log plot, which are first estimated by least-squares fits of 17 points around the respective pivots. The averaging is done over a suitable range, i.e. a regime with constant slope if available and between 200 and 1000 μm otherwise. Indicated errors represent root mean square deviations from the mean local slope. Hence, a large value would indicate a less fractal object.

The mean fractal dimension of the vasculature was estimated over three regions as indicated in Fig. 5. The center of the tumor, for which $\langle d_f \rangle(C) = 1.59 \pm 0.02$ was obtained. This central region reaches up to a boundary region (B), a 400 μm wide band along the perimeter, centered at the invasive edge. The width of the band is chosen deliberately according to the growth factor radius,
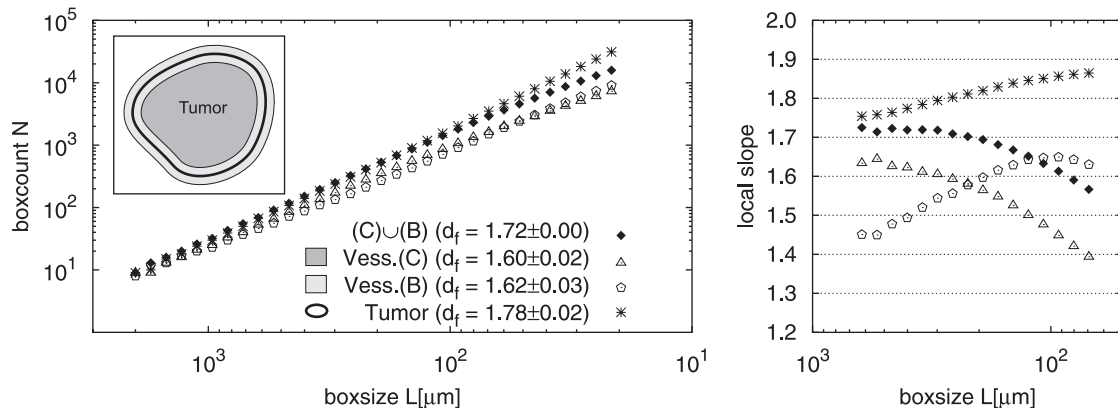
Fig. 5. Fractal dimension analysis of the base case tumor via boxcounting. Left: Boxsize vs. boxcount logarithmic plots. (C) denotes the vessel network in the tumor center region. This fills the space up a 200 μm wide band centered at the invasive edge around the tumor (B). (C) ∪ (B) contains all vessels in the union of region (C) and (B). "Tumor" denotes the viable regions of the tumor. Right: Local slopes of the curves on the left.
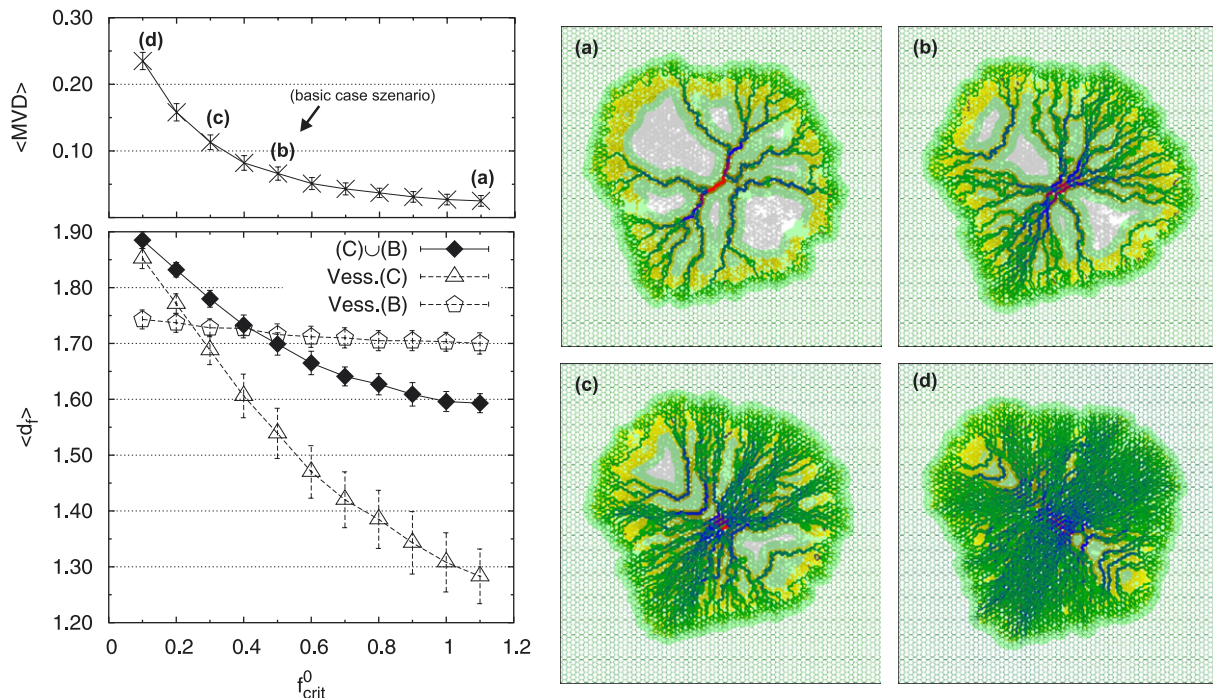

Fig. 6. Fractal dimension in dependence on critical shear stress. Left: In analogy to Fig. 5, (B) denotes a 200 μm wide band around the invasive edge, (C) the central region, and (B ∪ C) the entire tumor vasculature. The MVD is averaged over 20 tumors and over a disc with $r = 1.6$ mm. The data were generated by running simulations with $f^{(c,max)}$ ranging from 0.1 to 1.1 Pa. Right: Four configurations are shown with critical shearforces $f^{(c,max)} = 1.1, 0.5, 0.3, 0.1$ Pa. The labels on the left figure correspond to these configurations. The fractal dimension ranges from 1.61 to 1.82.

such that the exclusively angiogenesis dominated remodeling is captured. There $\langle d_f \rangle (B) = 1.63 \pm 0.03$ was obtained. The fractal dimension of the complete tumor vasculature turned out to be $\langle d_f \rangle (C \cup B) = 1.71 \pm 0.01$, and that of the tumor $\langle d_f \rangle (Tumor) = 1.78 \pm 0.02$. These values are lower than those reported in Bartha and Rieger (2006) for the simplified model, but are closer to the value $d_f = 1.81 \pm 0.04$ found experimentally for carcinoma (Gazit et al., 1995; Baish and Jain, 2000).

Fig. 5 also shows that the local slopes for the tumor and its vasculature are very similar for box-sizes greater 350 μm. This can be explained by considering that all tumor vessels have cuffs of viable TCs around themselves

with a diameter of ca. 200 μm- twice the oxygen diffusion radius. Further away from vessels no living TCs exist. Therefore in the large box limit ($L \gg 200$ μm) vessels and TCs will touch mostly the same boxes and thus yield similar fractal dimensions.

3.3. Parameter variations

Further experiments reveal that the fractal dimension of the tumor vasculature is apparently not a universal constant. Multiple simulations were performed where the maximum critical shear force ranges from 0.1 to 1.1 Pa, producing tumors with decreasing internal MVD. Fig. 6

shows the results. The fractal dimension of the boundary $\langle d_f \rangle(B)$ remains constant around 1.68, whereas the dimension of the complete vasculature $\langle d_f \rangle(B \cup C)$ ranges from 1.61 to 1.83. Naturally $\langle d_f \rangle(B)$ is a lower bound because it corresponds to the case where no internal vessels are present. With increasing density the dimension is dominated by the internal vasculature. The dimension of the tumor follows that of the vasculature for reasons already discussed.

In order to study the relation to conventional random bond percolation, simulations were performed with critical shear stresses ten times higher than normal $f^{(c,max)} = 5\,\text{Pa}$. At normal values for the collapse probability $p^{(c,max)} = 0.01$, this would remove all vessels almost instantly when the tumor grows over them. As shown in Fig. 7 there is however a sharp transition at $p^{(c,max)} = 0.001$ from the absence of vessels in the center to configurations where no vessels collapse at all. Note that the high value essentially inhibits the shear force stabilization mechanism which means that collapses are purely random and uncorrelated with flow. Visually this can be seen by the absence of the imposed flow direction. As a consequence all central vessels had the same probability to collapse by the end of the simulation, namely the probability to collapse until the stable radius is reached. Therefore the results here are in agreement with conventional percolation theory as described in the discussion Section 5.

3.4. Simplifications

In the following the effect of several simplifications toward the model discussed in Bartha and Rieger (2006) are discussed: replacing the viscosity term with a constant or purely radius dependent value; settings the vessel collapse probability and critical shear force to step functions; generating perfused sprouts instantly; and setting the oxygen source strength constant.

Blood viscosity: To compare the effect of different models for blood viscosity, we set the blood-oxygen content constant to the initial hematocrit value: $c_o^{(B)} = H^{(0)} = 0.45$. Consequently, this removes the large scale variations in the oxygen field and thus produces symmetric tumors. With this modification multiple simulation runs were performed with

 (i) the original viscosity model including hematocrit and blood phase separation;
(ii) a viscosity term which was derived from *in vitro* data (Gödde and Kurz, 2001) and which depends only on the vessel radius $\eta = \eta^{(plasma)}\eta^{(rel)}(r)$. (see Fig. 8);
(iii) the vessel viscosity set to the constant blood plasma viscosity. $\eta = \eta^{(plasma)}$.

The result is shown in Fig. 9. While the cases (ii) and (iii) do not differ significantly, the tumor MVD in (i) is ca.
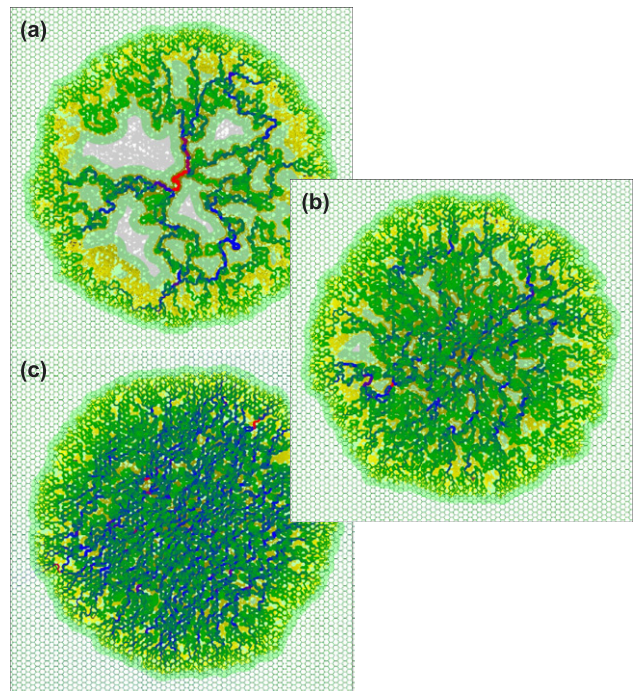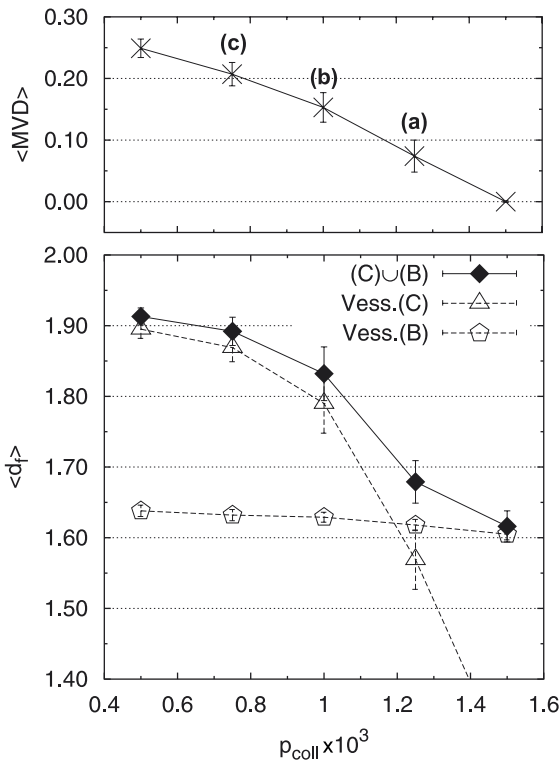

Fig. 7. Fractal dimension for tumors with uncorrelated vessel collapses. Left: (B) denotes a 200 μm wide band around the invasive edge, (C) the central region, and (B ∪ C) the entire tumor vasculature. Fractal dimension estimates for the three regions are shown, where $p^{(c,max)}$ ranges from 0.5×10^{-3} to 1.5×10^{-3}. Furthermore critical shear force and collapse probability were set constant within the tumor with $p^{(c)}$ as indicated $f^{(c,max)}$ was set very high to 5 Pa in order to reduce shear force correlation of collapses to an insignificant amount. Right: Three configurations are shown with $p^{(c,max)} = 1.25, 1.00, 0.75 \times 10^{-3}$ for (a),(b),(c) respectively.

two times lower than in (ii),(iii). This is unexpected but we think the following is a plausible explanation: The viscosity in (i) rapidly decreases by 50% from $r = 5$ to $20\,\mu m$, i.e. from outside to inside the tumor, whereas it changes less drastically in (ii) and (iii). The total flow into the tumor is generally limited by the flow resistance of the surrounding network. Let us assume a prescribed constant in-flow $Q =$
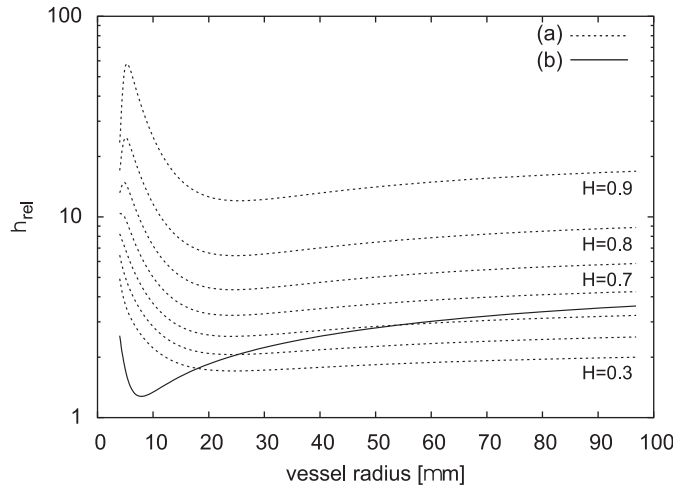

Fig. 8. Plot of the relative viscosity as a function of the vessel radius: (a) according to the formula derived in Pries et al. (1994), evaluated for hematocrit values $H = 0.3–0.9$; (b) data derived from in vitro measurements—see Gödde and Kurz (2001). Used here for the simplified model without hematocrit.

$N\,q \propto N\,f\,r^3/\eta$ which has to be supported by N vessels threading the tumor. Thereby assuming homogeneous flow-rate q, radius r, and shear force f. Let us further assume that f is identical to $f^{(c,max)}$. Then it is easy to see that the number of remaining vessels is proportional to the viscosity η.

Increasing the critical shear stress from 0.5 to $f^{(c,max)} = 1.0\,Pa$ drops the MVD back to the level of the base-case at the cost of increased flow rate and shear stress in the vessels. Fig. 9 shows respective averaged curves. Apparently there is no fundamental change in vessel morphology. This is also reflected by fractal dimension analysis where the mean dimensions only differ at most by 3%. Thus it is reasonable to assume that for the purpose of morphological studies an effective constant blood viscosity—ca. twice the plasma viscosity—can be used.

Vessel collapse: In the base-case both the collapse probability $p^{(c)}$ and the critical shear force $f^{(c)}$ are modulated by the function g_1 which introduces an explicit location dependency. In the following we present two cases with differently designed functions which might be equally well suited models. With $p^{(c)}$, we refer to the collapse probability of unstable ($f < f^{(c)}$ and $r < r^{(stable)}$) normal perfused vessels.

(i) Denotes the base-case where g_1 has a torus-like profile, as shown in Section 2.2. And where $p^{(c)}$ is additionally multiplied by a vessel-radius dependent term.
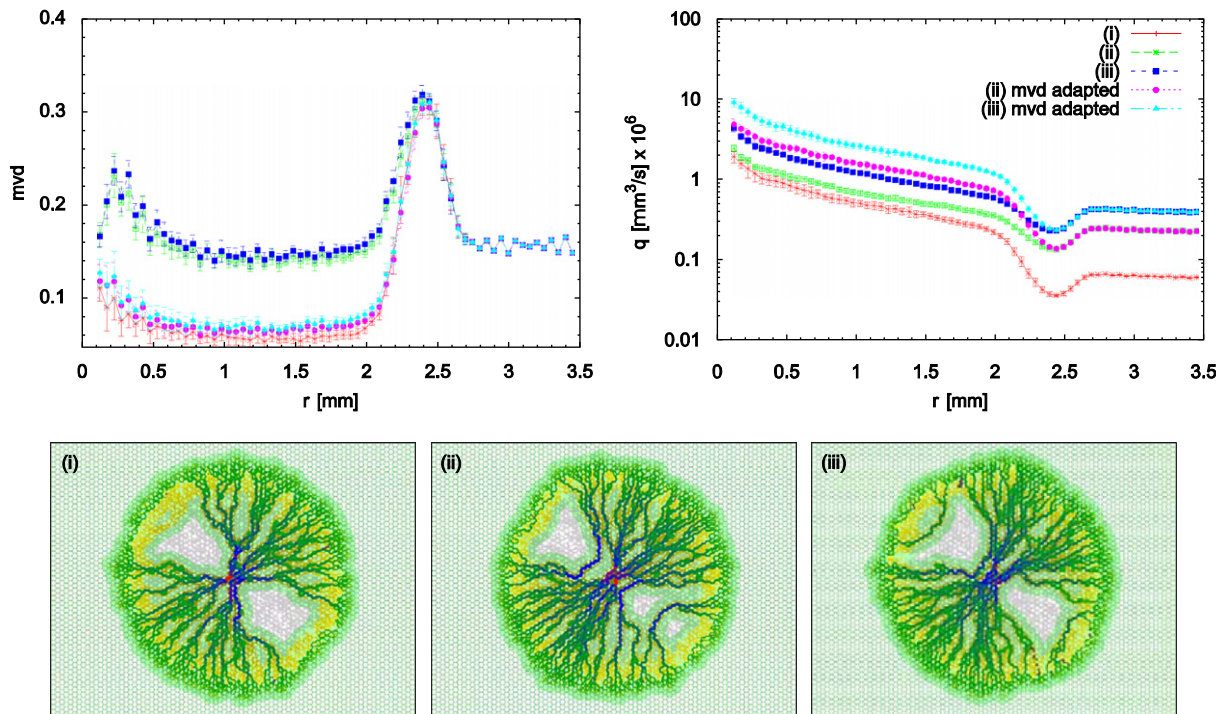

Fig. 9. Comparison of viscosity functions. Top: Shown are radial MVD and flow rate curves for different viscosity models and parameters at $t = 1000$. "adapted mvd" denotes data where the critical shear force has been tuned such that the MVD matches that of the original model. Bottom: Shown are snapshots of tumors of the adapted configurations. (i) Denotes the original flow model. All the simulation runs here where done with the oxygen field unaffected by the blood hematocrit content (ii) uses radius-only dependent viscosity formula of, Gödde and Kurz (2001) and (iii) assumes a constant value.

(ii) $f^{(c)}$ and $p^{(c)}$ assume constant values within the tumor and zero outside.

$$f^{(c)}(a, \boldsymbol{x}) = f^{(c)}(\phi, x)$$
$$= f^{(c,max)} \cdot \theta(x_T(\phi) - x), \tag{14}$$

$$p^{(c)}(a, \boldsymbol{x}) = p^{(c)}(\phi, x)$$
$$= p^{(c,max)} \cdot \theta(x_T(\phi) - x) \cdot \theta(r^{(stable)} - r_a), \tag{15}$$

where θ is the step function, x is the distance to the center, ϕ the polar angle and r_a the vessel radius. Beside the dependence on the distance to the tumor, the linear dependence on r_a has also been replace by a step function, such that the collapse probability becomes 0 instantly once $r_a \geqslant r^{(stable)}$. Without changes to other parameters this results in decreased central MVD. Therefore $f^{(c,max)} = 0.25\,\text{Pa}$ is chosen, which is 1/2 of the normal value. $p^{(c,max)} = 0.01$ is left unchanged. In the latter case no significant difference to the base case scenario could be observed. Radial curves differ at worst by 10% and the mean fractal dimension is also in agreement within the error bounds.

(iii) $f^{(c)}$ decays from $f^{(c,max)}$ at the center of the tumor to 0 at the invasive edge. For $p^{(c)}$ the simple form from (ii) is chosen.

$$f^{(c)}(a, \boldsymbol{x}) = f^{(c)}(\phi, x)$$
$$= f^{(c,max)} \cdot \max\{0, 1 - x/x_T(\phi)\}, \tag{16}$$

$$p^{(c)}(a, \boldsymbol{x}) = p^{(c)}(\phi, x)$$
$$= p^{(c,max)} \cdot \theta(x_T(\phi) - x) \cdot \theta(r^{(stable)} - r_a). \tag{17}$$

In this case the original parameters work fine: $f^{(c,max)} = 0.5\,\text{Pa}$ and $p^{(c,max)} = 0.01$. Fig. 10 shows that compared to (i) and (ii) a smoother transition from the high-MVD boundary to the tumor center with low MVD is obtained. In an experiment not shown here this effect was enhanced by setting $p^{(c)}(a) \propto \max\{0, 1 - r_a/r^{(stable)}\}$. Further on, peripheral MVD has slightly increased since collapse events happen now closer to the center where the critical shear force threshold is high enough. Being directly correlated to the MVD other measurements such as oxygen level or tumor density exhibit similar behavior. The mean fractal dimension of the tumor vasculature is $\langle d_f \rangle = 1.80$.

Sprout migration: In analogy to our previous work, we also checked the results when "sprouts" instantly extend to the next vessel, possibly creating a perfused loop.

This simplified sprout model works as follows: Starting at a parent vessel, sites along a straight path are checked for a destination vessel. As before, the direction is determined by the local GF gradient at the starting site. A vessel connection is added, provided that all conditions for sprout generation—such that it has to be outside the tumor—are fulfilled for the starting site, and that the
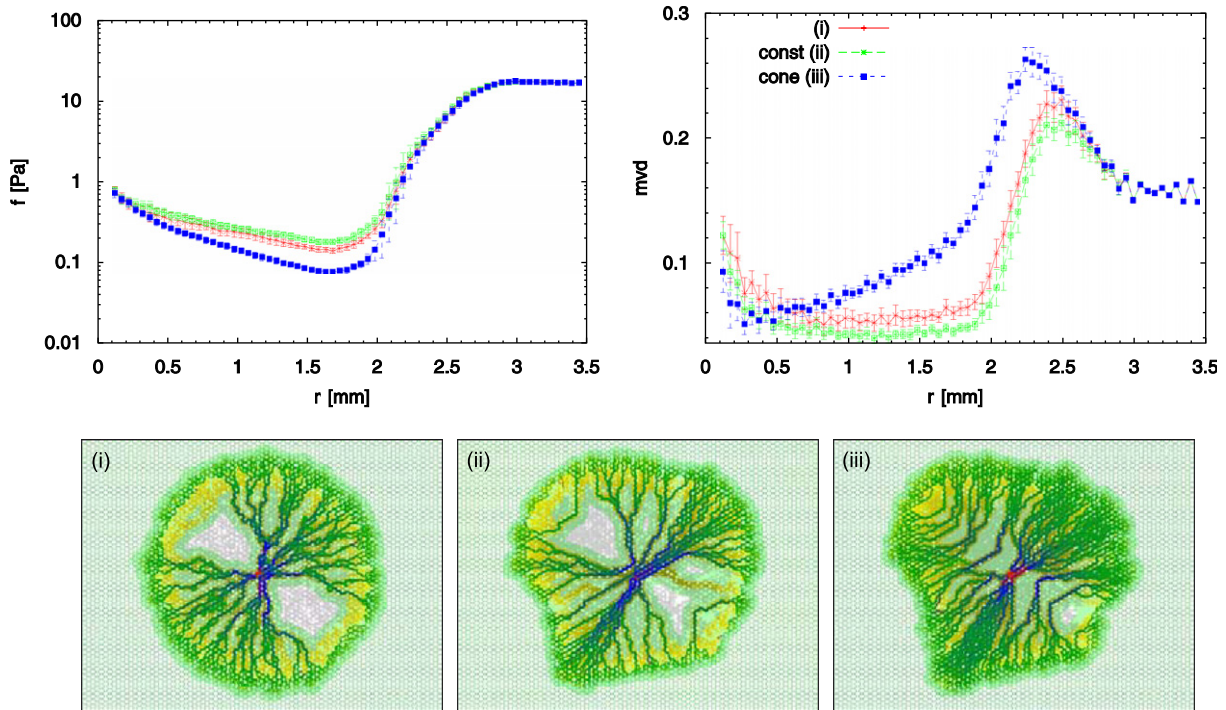

Fig. 10. Comparison of different dependencies of $p^{(c)}$ and $f^{(c)}$ on local system properties. Top: row shows mean shear force and vessel density by radial distance at $t = 1000$, (i) is the basic case model, (ii) has positive constant values for $p^{(c)}$ and $f^{(c)}$ inside the tumor, with the exception that $p^{(c)} = 0$ for $r \geqslant r^{(stable)}$ and (iii) has a linear decay from $f^{(c)} = f^{(c,max)}$ at $r = 0$ to 0 at the invasive edge. Notice how the MVD decreases much smoother toward the center. Bottom: shows snapshots of sample tumors.

destination site has less than three incident vessels. The resulting tumor's boundary regions exhibit ca 70% the MVD of the full model's tumors. Apparently the stronger requirements for vessel creation limit the degrees of freedom for the system's evolution. For example in the original model there is the possibility that two sprouts grow simultaneously and form a perfused wedge when they meet inside a hexagon. MVD correlated data vary accordingly, but otherwise no fundamental changes could be observed.

Oxygen field computation: Solving the O_2 diffusion equation with implicit source strengths can become expensive, in particular in three dimensions. Therefore we also performed simulations using a simplified model. Instead of solving $\Delta c_o - \kappa c_o + \alpha(c_o^{(B)} - c_o) = 0$, we do now consider

$$\Delta c_o(\mathbf{x}) - \kappa^{(M)} c_o + \alpha c_o^{(B)} = 0, \qquad (18)$$

where the coefficient κ equals the tissue consumption $\kappa^{(M)}$, disregarding the tumor. The occurrence of $c_o(\mathbf{x})$ is omitted in the source term which means that O_2 is produced at a fixed rate. (18) could be efficiently solved by a Greens-function approach, in analogy to our solution of the GF distribution. In the present case, q_0 is simply a prefactor that scales the field values globally, and it is chosen to get the mean O_2 $\langle c_o \rangle = 0.2$. The tumor proliferation threshold remains at the original value $\theta_o^{(prol)} = 0.29$.

As a consequence the O_2 level increase from normal MVD to high MVD is overestimated by ca. 50%. Fig. 11 shows snapshots from two runs at $t = 1000\,\text{h}$.

(i) shows a snapshot from the full model. To facilitate comparisons the effect of hematocrit on O_2 has been disabled, i.e. $c_o^{(B)} = H^{(0)}$;

(ii) shows a snapshot from the simplified model. As can be seen the tumor grows slower and develops and elliptical shape. Here TCs produce GF only if $c_o(\mathbf{x}) < \theta_o^{(prol)}$. Due to the higher O_2 level, the outer band where TCs are allowed to proliferate—and do not produce GF—is almost as wide as the GF radius. Therefore the GF influence region—indicated by a bright green background—does not reach as far into the tissue as in (i), leading to slower vessel generation and thus slower tumor growth. Depending on parameters, the growth of the tumor may even come to halt in the beginning of the evolution when the O_2 level increases above $\theta_o^{(prol)}$ for all TCs in the nucleus. In the full model no reasonable parameter set allows such increase in O_2 and therefore this behavior has never been observed;

(iii) shows snapshots from the simplified model—modified so that TCs always produce GF. Naturally the GF influence zone now has the largest possible extend, leading to continuous neovascularization and virtually undisturbed Eden-like tumor growth. Overestimating
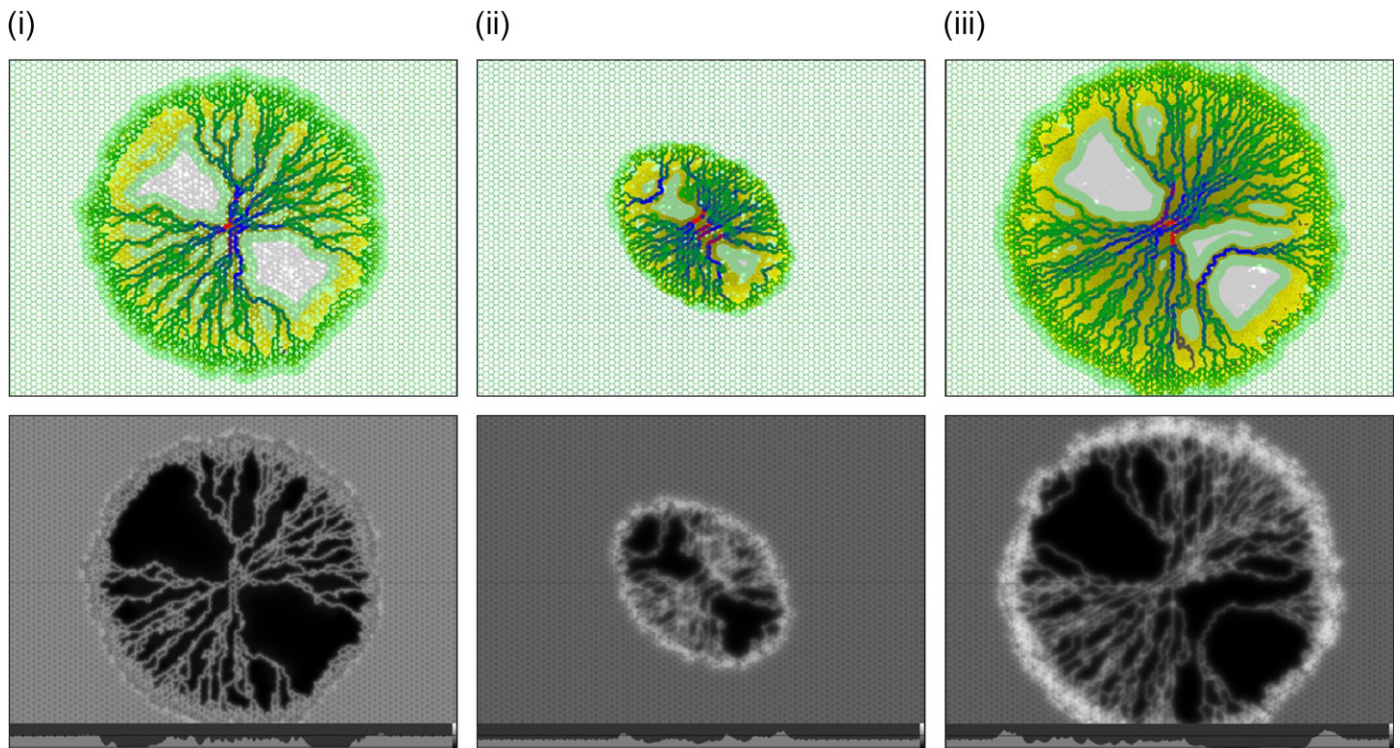

(i)   (ii)   (iii)

Fig. 11. Comparison of different oxygen and proliferation models. The top row shows vessel, tumor, gf-influence configurations. The lower row shows associated oxygen fields and central cross section, (i) is the full O_2 model for $c_o^{(B)} = H^{(0)} = const$, (ii) is the simplified O_2 model with constant source strength, (iii) is the simplified model (ii) with the addition that TC always produce GF.

the O_2 levels also the effect of making the model more robust regarding the choice of the TC proliferation threshold $\theta_o^{(prol)}$. This leads to the observations that tumor (iii) is denser than tumor (i) and grows slightly faster. The O_2 level in (i) increases by mere 10% at the high MVD periphery, leaving not much choice for $\theta_o^{(prol)}$ because at low values TCs can proliferate quickly along the original vessels which can create holes as seen in Fig. 11 (i). At high values the tumor might not proliferate at all.

Simplifications combined: Measurements from tumors with simplifications combined are shown in Fig. 12. In these simulations blood viscosity is set constant $\eta = \eta^{(plasma)}$, collapse probability and shear force are also set constant according to (14), oxygen computations are done with the simplified model from (18), and all TCs produce GF. Parameters, $f^{(c,max)}$ and $p^{(c,max)}$ in particular, are equal to the settings in the full model simulations. To get better estimates for data near the invasive edge, it is compared to the basic model without hematocrit affecting oxygen levels $c_o^{(B)} = H^{(0)}$.

All modifications combined lead to changes in many measurements. Most of which have already been discussed in the examples above. For example the almost 10-fold increase in flow rate due to reduced viscosity, increased oxygen in high MVD regions due to constant source strengths, faster and denser tumor growth due to better oxygen supply. Not observable before is an apparent difference in vessel morphology. Note the tendency to form compact straight bundles of 3–8 vessels. Vessels in snapshots of the basic case—denoted (i) here, see Fig. 3 for instance do not seem to have this property, instead those exhibit many small weakly perfused loops and cross-links. Radial curves (ii) seem to reflect this also by an overall increase in shear force. Most likely weakly perfused vessels in (i) survive long enough until the relatively thin ring of high collapse probability has moved further outwards. If so they can contribute to the shear force measurement such that the mean values are lowered. Fractal dimension analysis also indicates different morphological features. The mean vasculature dimension has increased to $\langle d_f \rangle = 1.77$, although the central MVD has not increased significantly. Fig. 12 also shows results from box-counting analysis of a single sample tumor. Over a small range the local slope reaches peak values of ca. 1.82.

4. Drug flow modeling

This section discusses modeling, and results, of simulated drug flow through the tumor vasculature. The mathematical model for drug flow is based on McDougall et al. (2002), where it was demonstrated how the concentration profile of a tracer substance flowing through a vascular network can be tracked. The drug flow model is designed on top of the already established network model.
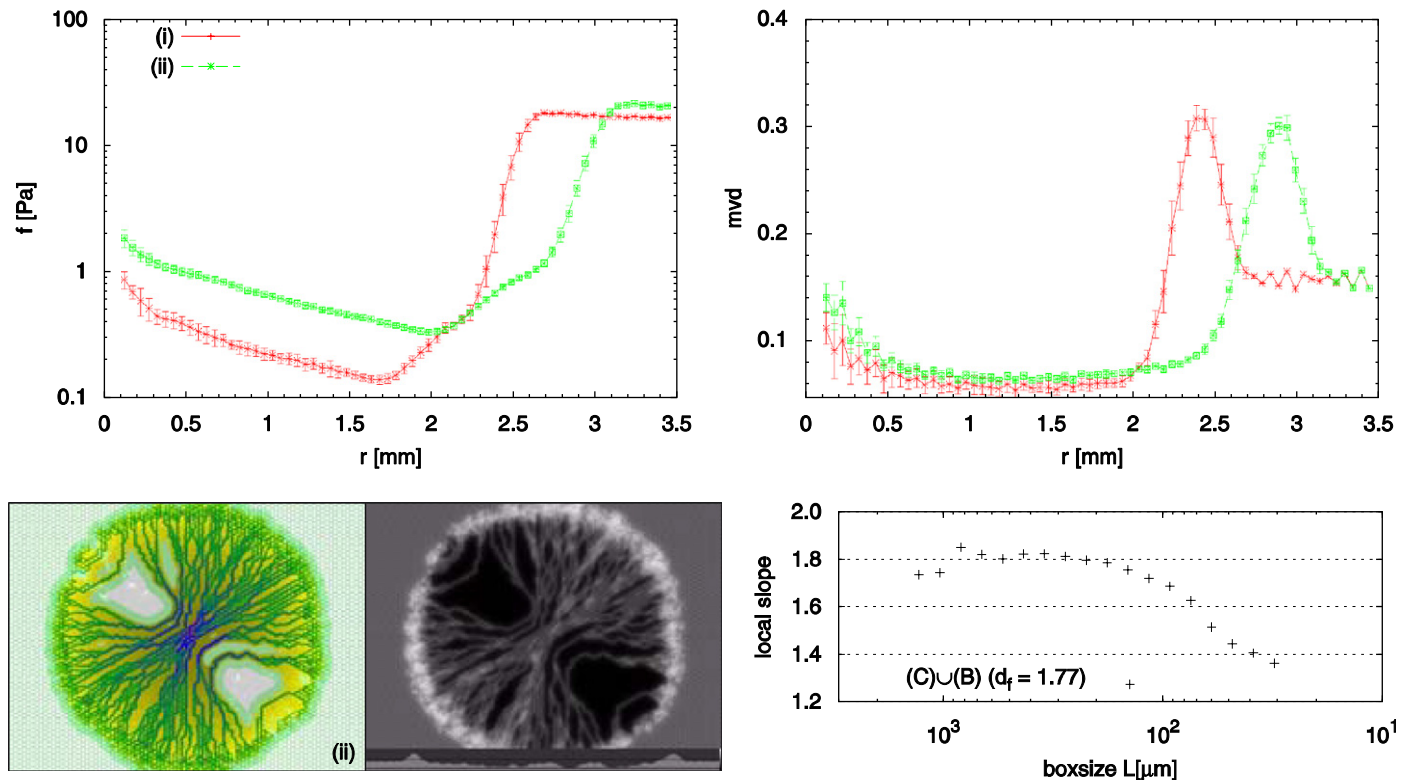

Fig. 12. Measurements from simulations with simplified viscosity, oxygen computations and vessel collapse model. Top row shows radial curves for shear force and MVD, (i) is the original model and (ii) the simplified version. The bottom row shows snapshots on the left. The right-hand side shows local slopes from boxcounting analysis for the complete tumor vasculature.

Hemodynamic parameters, such as flow rate are precomputed (taken over from the results of the tumor simulation). The network is completely static during the simulation, which is reasonable as as the drug injection does not last longer than one hour. An iterative algorithm first propagates drug mass from vessels to downstream nodes, followed by a second pass where drug is distributed among the outflow vessels. Thereby mass conservation is strictly enforced. One such iteration corresponds to a certain time-step δt. A detailed description is given in the following.

4.1. Model definition

First, node tupels (i, j) which identify vessels now reflect the flow direction by requiring that $p_i \geqslant p_j$. Geometric and hydrodynamic properties q, l, r, p have meanings as before and their values are static. With I_i and O_i we denote the inflow- and outflow-vessels attached to a node i. In addition to the ideal pipe-flow model, a number of further assumptions are made: Drug is moved downstream with the average flow velocity $v = q/[\pi r^2]$ neglecting radial velocity differences. For each vessel, the simulation tracks a single drug-containing cylindrical subsection. Let $u \in [0, l)$ be its start at the upstream end, measured along the central vessel axis. The downstream end is given by $d \in (u, l]$. The occupied volume is thus $V = (d - u)\pi r^2$, and it is assumed that the drug mass m inside this volume is always homogeneously distributed at the concentration m/V. Thus the description of the concentration profile inside a vessel segment is limited to a single square pulse. This does not appear to be a problem, but when necessary, segments can be subdivided to gain a suitable resolution.

For each time step δt the following is done: First, for each vessel $a = (i, j)$ which has drug $m > 0$ drug is moved downstream by the distance Δx. Let $t' = t + \delta t$, then:

$$\Delta x = q/[\pi r^2]\delta t,$$
$$u^{t'} = u^t + \Delta x,$$
$$d^{t'} = d^t + \Delta x.$$

The volume is then pruned at the end of the vessel, and the lost drug mass is accounted to the attached node. This mean if $d > l$ and $u < l$ the drug propagation into the nodes is as follows:

$$\Delta m = m^t/V \cdot [d^{t'} - l]\pi r^2,$$
$$m^{t'} = m^t - \Delta m,$$
$$m_j^{t'} = m_j^t + \Delta m,$$
$$d^{t'} = l.$$

If the time step is large enough it can happen that a vessel is completely drained of drug $u^{t'} >= l$. Care must be taken that state variables are kept consistent. Instead of the steps above, all mass is transferred to the node: $\Delta m = m^t$, and the drug start and end variables are reset to $u^{t'} = d^{t'} = 0$.

In a second stage it is looped over all nodes $i \in N$ that have drug $m_i > 0$. This drug is now propagated further downstream into connected vessels. At boundary nodes, drug may be introduced by adding the contribution $\Delta m = (\sum_{a \in O} q_a - \sum_{a \in I} q_a)C^{(in)}\delta t$ from the in-flowing blood volume. The distribution at branching points assumes perfect mixing, i.e. the nodal drug mass is split among outflow vessels proportional the blood volume that flows into a vessel. Let Q be the total out-flowing volume: $Q = \max[\sum_{a \in O_i} q_a, \sum_{a \in O_i} q_a]$. This formal description respects that the correct value has to be computed for boundary nodes where Kirchhoff's law is violated due to exchange with the environment. For internal nodes Q is of course equal to $\sum_{a \in O_i} q_a$. Then for all vessels $a \in O_i$ drug mass is updated according to

$$m_a^{t+1} = m_a^t + q_a/Q \cdot m_i^{t'}.$$

Furthermore u_a is set to 0, because drug just entered at the upstream vessel junction. Once again care must be taken to ensure a consistent system state at the end of the iteration. In our implementation the downstream drug end must move forward to $d_a^{t+1} = q_a/[\pi r_a^2] \cdot \delta t$ if the vessel was empty. Note that in this case it has also been $d_a^t = 0$. The time step δt must be chosen carefully to ensure that the location of the drug remains consistent with the network structure. During a time step drug can only move as far as the length of a vessel. Therefore it must be ensured that the in-flowing blood volume $q\delta t$ is less than the volume of the vessel: $q\delta t <= l\pi r^2$. The largest possible δt is thus

$$\delta t = \min_{a \in V}\left\{\frac{l_a \pi r_a^2}{q_a}\right\}. \tag{19}$$

Drug uptake by the tumor is not considered here. It was incorporated in McDougall et al. (2006) in a very crude way: Drug was instantly removed once it reached the tumor. This is not feasible here, since the goal is to study the concentration inside tumor and see if there are spots that are unlikely to be supplied by sufficient drug. It should be possible with some more numerical effort to include a diffusion process through the vessel wall in the line of the O_2 concentration computations presented before. But for simplicity and the lack of experimental data this has not been done yet. As a consequence the intravascular drug concentration here can only predict an upper bound to the real concentration.

4.2. Results

Here we discuss results for two configuration types: (i) the base-case (Fig. 3); (ii) nearly shear force uncorrelated systems with $p^{(c,max)} = 0.001$ and $f^{(c,max)} = 0.5$ (Fig. 7).

In both cases first a preprocessing step was applied. Vessels outside a circular region were removed, such that a band of approximately 1 mm width remained around the tumor. Doing so ensures that drug arrives evenly at the invasive edge, which would not be the case if the network spreads over the entire rectangular domain. Fig. 13 shows

the flow velocity which is of the order of 0.5 mm/s. Regular capillary networks have high flow resistances and do not support increased flows inside the tumor. On the contrary, the dilation causes slower velocity, due to the preservation of mass (Fig. 14). Thereby (i) and (ii) show similar behavior. Simulations were done with injection durations $t^{(in)}$ ranging from 2 to 60 s. The injected concentration was always set to $C^{(init)} = 1$. Fig. 15 shows a sequence of concentration profiles for the hexagonal lattice base-case (i) and $t^{(in)} = 60$ s. Drug enters at the bottom left boundary, and flows toward the tumor. The concentration at the drug "front" shows an increasingly smooth transition. That is because at branching points, the front does not arrive through all inflow vessel simultaneously. Thus drug containing blood is mixed with "clean" blood, decreasing the concentration in out-flowing blood. After 60 s tumor vessels are almost completely saturated with drug. A prolonged injection would keep the system in a fully saturated steady state. The second half of the sequence shows how blood flows out of the tumor after the injection ends.

For shorter injection times, flow results naturally give a similar picture (no image sequence shown here). A compact short burst of approximate length $vt^{(in)}$ flows unhampered in diagonal direction through the tumor. However, the maximum concentration can be significantly decreased due to the mentioned mixing effects. For example in the extreme case where $t^{(in)} = 2$ s, the number of vessels where the concentration $C > 0.5$ is reduced to 30%.

Fig. 16 shows averaged measurements of case (i). The plot on the left indicates the percentage of vessel network length that was exposed to a drug concentration greater than the value on the x-axis. The data are given for injection times $t^{(in)} = 10, 20, 30$ s. For the 30 s injection, 90% of the vascular network was exposed to the maximum possible drug concentration $C^{(init)} = 1$, while all vessels were exposed to at least a concentration of $C = 0.9$. This simply reflects that the systems was nearly saturated with drug, which is also evident by the snapshots.

The right plot in Fig. 16 shows the percentage of vessel network length for which the concentration was larger than a threshold C_t for a total period greater than the value indicated on the x-axis. The data is again given for several injection times. For $C_t = 0.5$ and $t^{(in)} = 60$ s the curve has a step function profile, whereby the drop occurs at $t = 60$ s. This point in time corresponds in good agreement to the duration in which the high concentration "pulse" passes through the tumor. The concentration at a fixed location increases (decreases) smoothly over time before (after) the plateau of saturation. This means that the lower the concentration threshold, the longer the exposure times. Therefore curves for lower thresholds show "tails" beyond the saturation period. Prolonging the injection interval by Δt would increase the time where the system is in a saturated steady state, thus shifting the exposure time curves uniformly by Δt to the right. This is clear since the time that the system remains in steady state is irrelevant. The curves for $t^{(in)} = 10$ and 30 s show the effect very well that the drop is simply shifted to the end of the injection period, thereby preserving the trails.
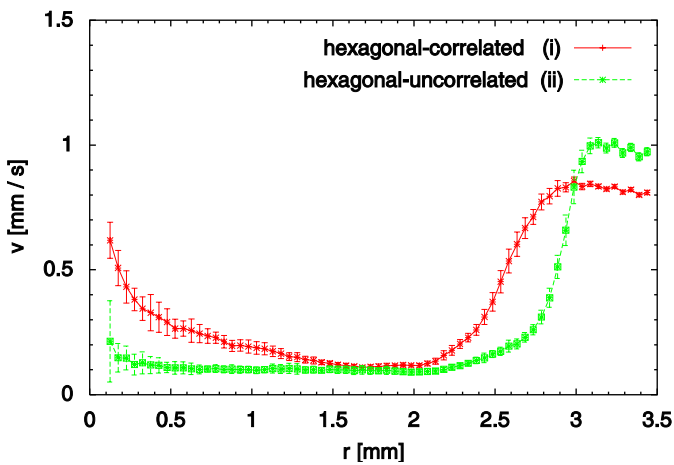

Fig. 13. Radial measurement of the mean flow velocity $v = q/[\pi r^2]$. (i) denotes the base-case (ii) a shear force uncorrelated system with random collapses (Fig. 7).
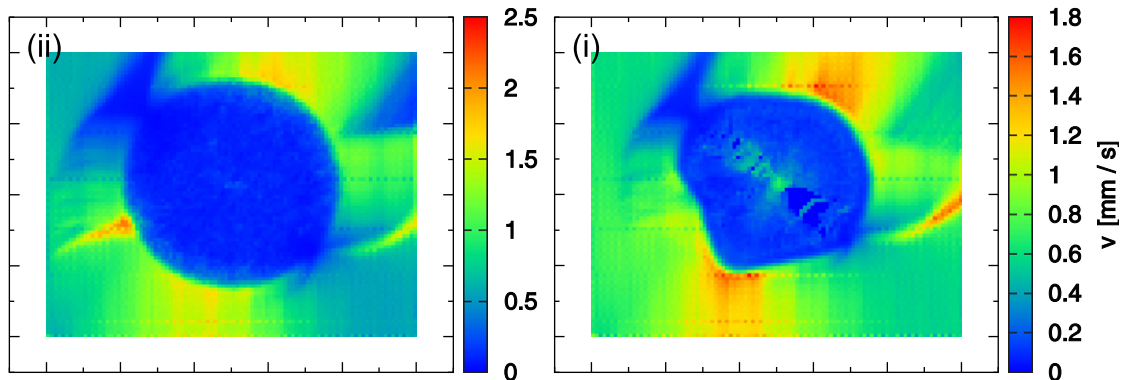

Fig. 14. Spatial distribution of the blood flow velocity for (i) the base-case scenario (Fig. 3) and (ii) the shear force uncorrelated case (Fig. 7b). Both plots show an average over 20 simulation runs at time step $t = 1000$ h, the represented area being 12×10 mm². Compared to normal tissue, the flow velocity is reduced in the tumor. The flow increases in (i) toward the center due to the star like structure with fewer vessels there.
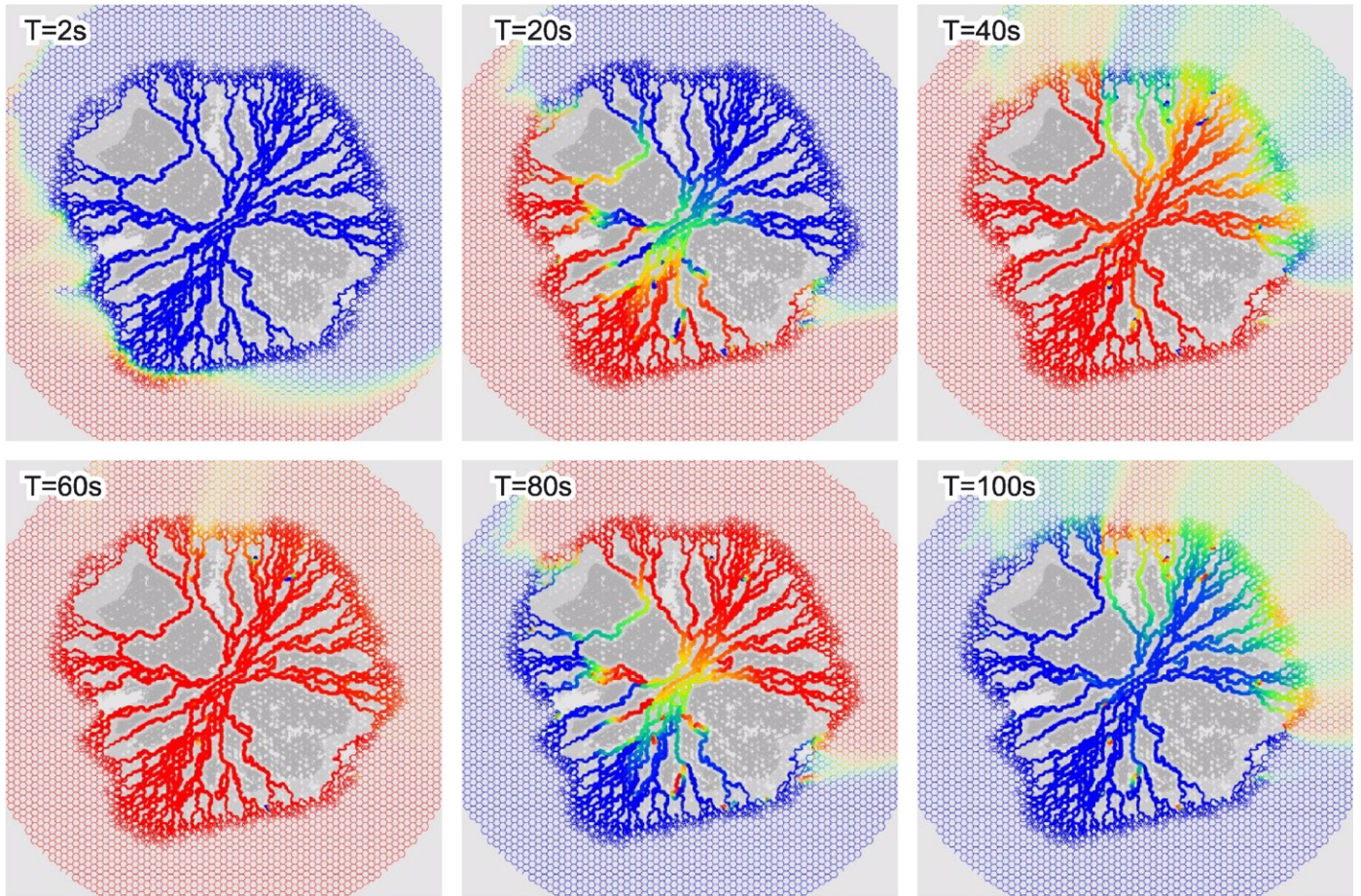
Fig. 15. Concentration profiles for an injection of $t^{(in)} = 60\,\text{s}$ into the hexagonal base-case vasculature (i). The color code ranges from red at $C = 1$ over yellow and green to blue at $C = 0$. Light gray area represents viable tumor tissue, darker gray represents dead tissue. Drug reaches the invasive edge within the first 2 s. At the middle of the sequence, the tumor becomes saturated with drug, except for a few tiny spots. Note how the concentration drops gradually in most vessels as an effect of mixing with "clean" blood.
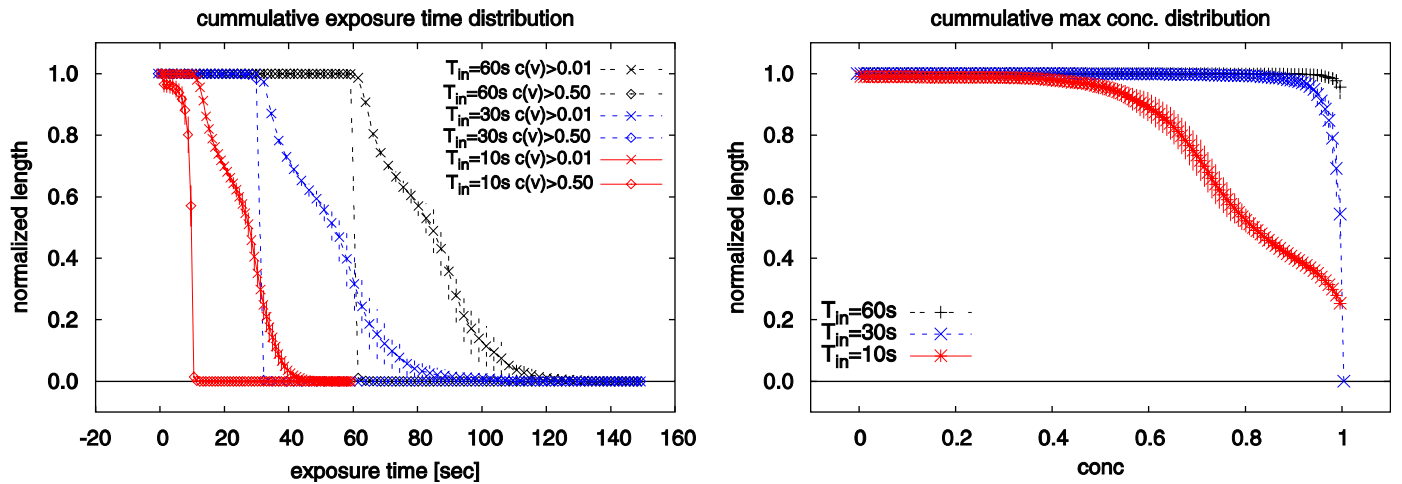

Fig. 16. Quantitative measurements of the base-case (i) for various $t^{(in)}$. Right: The plot indicates the percentage of vessel network length that was exposed to a drug concentration greater than the value on the x-axis. When the system has time to reach a steady state all vessels become exposed to $C(v) = 1$, thus producing a constant line in the plot. Left: The plot shows the percentage of vessel network length for which the concentration was larger than C_t for a total period of more than indicated on the x-axis. The steep drops occur at the end of the injection duration. Naturally the mean time where vessels are exposed to $C > 0$ is on the order of $t^{(in)}$ plus the time it takes to clear the tumor of drug, depending on the vascular morphology and flow rates.
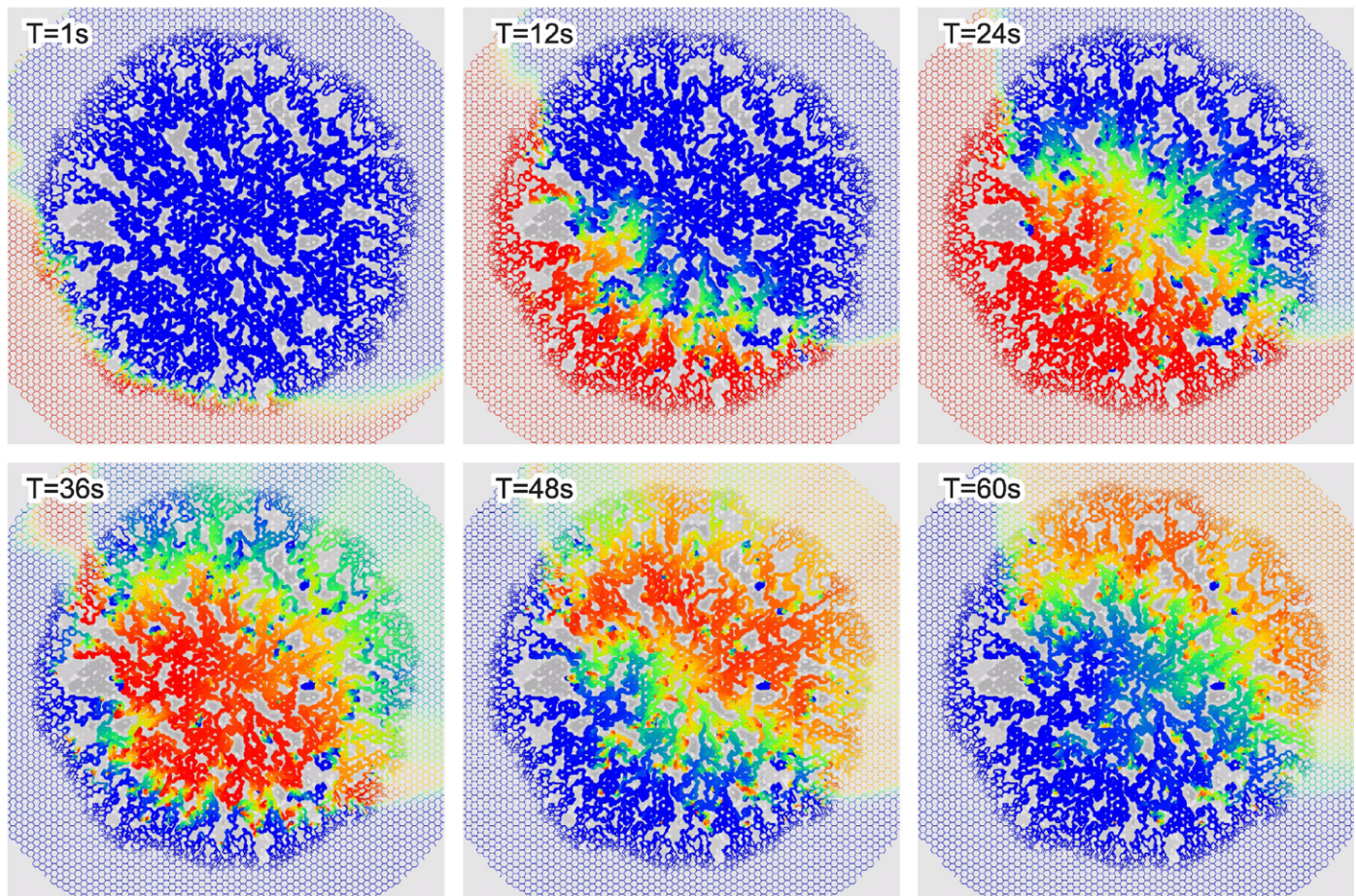
Fig. 17. Concentration profiles for an injection of $t^{(in)} = 60\,\text{s}$ into the hexagonal shear force uncorrelated vasculature (ii). The morphology created by random collapses inside the tumor exhibits more poorly perfused loops than any other vasculatures. As can be seen a few vessels have not been reached by the injected drug during the whole simulation period. The qualitative behavior is otherwise in good agreement with the run presented in Fig. 15.

Plots for the uncorrelated case analogous to Fig. 16 are not shown here because they are qualitatively as well as quantitatively very similar but exhibit a few unreachable loops. This is reflected in a smoother drop in the maximum concentration curve: ca. 80% of the vasculature had a concentration greater than 0.8. The exposure time plot showed slightly smoother drops at the injection times and a longer trail but is otherwise identical to Fig. 16.

Fig. 17 show concentration profile sequences for the remaining cases. Most remarkable in the uncorrelated case (ii) is the occurrence of small unreachable loops. It can happen when vessels survive which are oriented perpendicular to the global pressure gradient given by the boundary conditions. Flow rates in these loops are consequently drastically reduced.

5. Discussion

We have shown that the basic predictions of the model introduced in Bartha and Rieger (2006) are very robust against different sophistication levels of mathematical modeling that we investigated: The base case scenario, in which model parameters are chosen to the best agreement with experimental data for melanoma (Döme et al., 2002), the tumor compartmentalizes after a short time into three regions: A well vascularized peritumoral plexus with an MVD that is 2–3 fold larger than the normal tissue MVD, a well perfused peritumoral region and a necrotic core with low MVD and only a few thick vessels threading the tumor, which are covered by a ca. $100\,\mu\text{m}$ thick cuff of tumor cells. Oxygen levels are therefore extremely low in the tumor vessel. The fractal properties of tumor vasculature are substantially different from the normal vasculature, with estimates for the fractal dimension that are lower than that of the normal capillary network. Their characteristics have their origin in the vessel collapse processes and therefore also depend sensibly on collapse probability and critical shear force. Concerning the hydrodynamic blood flow patterns our model shows substantially reduced pressure gradients and shear flow in the tumor vasculature, although the blood flow rate is increased in the extremely thick vessels in the tumor center. The tumor radius grows linearly in time, which is natural as long as TC proliferation is confined to the tumor surface region and no growth inhibition effects, like solid stress, are incorporated.

These are robust features that are characteristic for the model we have studied here *and* for the simplified model of Bartha and Rieger (2006). A few differences between the two versions occur only on a smaller scale.

Calculating oxygen sources implicitly, i.e. driven by concentration gradients between blood and tissue, instead of assuming a constant source strength as in Bartha and Rieger (2006), have the following effect: Surface TCs can proliferate in the original vasculature while cells behind the invasive edge now suffer from hypoxia due to increased metabolic demand inside the tumor. They are thus secreting GFs to induce angiogenesis. If the oxygen threshold for proliferation is of the order of the average tissue-O_2 levels ($\theta_o^{(prol)} \approx \langle c_o \rangle$), the model predicts a strong dependency on the micro-scale O_2 variations and therewith also on local vascular morphology. The model with explicit sources is more stable with respect to the proliferation threshold, since the O_2 level increases rather drastically in highly vascularized regions. However, by choosing suitable parameters, the vascular morphology of the model we studied here and the simplified version with constant source strength can be matched. Therefore to study the global features of tumor vasculature the crude approximations to O_2 diffusion fields may be used, in particular in numerically more challenging situations such as 3d simulations (Lee et al., 2006).

Progressively simplified blood flow computations alone have shown limited effects, mainly changes in the flow rates up to one order of magnitude could be observed within the tumor. Additional modifications of the collapse rules influenced the shape of the vascular network visibly, (Fig. 10.(ii) vs. Fig. 12.(ii)), but still the simplified model for blood flow can be can be used. Also the incorporation of the blood phase separation effect does not appear of significance for vascular morphology. When blood oxygen levels are allowed to vary proportional to hematocrit, the model predicts asymmetric growth depending on local hematocrit levels. Therefore if this aspect is to be neglected, performing computations according to Pries et al. (1994) with a constant hematocrit $H_0 = 0.45$ appears to be a good compromise.

Inserting completely new perfused vessels rather than generating migrating sprouts that eventually join to target vessels does not lead to substantial changes. The latter model version merely leaves more degrees of freedom for forming circulated loop. In two dimensions the space to grow in is confined between the initial vessels. Therefore incorporating a randomized sprout migration dynamics becomes relevant in a three dimensional model, where it is not a priori clear that sprouts migrating in a random direction hit a target vessel in a reasonable distance. Here chemoattractants and the size of the growth cone (i.e. extension of filopodia in real sprouts) become essential model features.

Concerning our drug flow simulations we have demonstrated that drug flows relatively well through all of the networks. Even in the extreme case—the uncorrelated system—an infusion time of the order of a few minutes is sufficient to saturate the vasculature with drug. Therefore our model predicts that blood-borne drug transport to and into tumors that grow within a homogeneously vascularized tissue is not limited by the particular morphology of tumor vasculature. Considering the underlying mechanisms that are responsible for this morphology in our model (and in real tumors) it is plausible that drug reaches (nearly) all parts of the vasculature: Shear force correlated vessel collapse naturally leads to elimination of weakly perfused vessels. In the case of random collapses, pressure gradients are still sufficient to drive blood through the vessels, but an order of magnitude slower.

In related work concerning modeling of tumor induced angiogenesis, McDougall et al. (2006) found that the morphology of tumor vasculature plays a crucial role in drug delivery and that changes to key system parameters could have big impact on the structure of the vasculature. The origin of this discrepancy with our conclusion lies in the different model assumption. As outlined in the introduction, they consider a strictly avascular tumor, where sprouts migrate toward the tumor, but are not allowed to enter it. The resulting vessel networks exhibit extremely high connectivity close to the tumor surface, however the involved angio-adaptation mechanisms lead to vasodilation of comparably few pathways. Depending on the model parameters, the number of high-throughput vessels, and their distance to the tumor varies sufficiently to lead to uptake rates which vary by several orders of magnitude.

In contrast to this we study here a type of tumors like melanoma, which are primarily vascularized by co-option rather than vessel ingrowth (Döme et al., 2002, 2007). For them, as we have demonstrated, a blood-borne "delivery problem" does not exist. This does however not automatically imply that drug reaches all tumor cells since neither drug transport through the tumor tissue nor drug uptake have been addressed (Minchinton and Tannock, 2006). Regarding tissue transport it is known that the difference between interstitial fluid pressure (IFP) and microvascular pressure (MVP) is low due to vessel leakiness. Since convective transport is driven by pressure differences, high IFP could pose a barrier to drug delivery (Hassid et al., 2006). On the other hand, leakiness and MVP-IFP gradients could lead to premature release predominantly in locally restricted regions around vessels where blood enters the tumor. Vessels in the outflow regions would thus be depleted of drug. Locally released drug would then be transported by IFP gradients out of the tumor. Furthermore drugs usually consist of large macromolecules. Their low diffusibility through the vessel wall and generally lower diffusibility than O_2 could lead to situations where sufficient O_2 reaches certain TCs to let them remain viable, but not enough drug reaches them to kill them off due to the lower diffusion radius. Thus we conclude that much more than the vessel morphology, processes like transportation out of the vessels through

convection and diffusion seem to be a key factor in successful drug delivery.

In future work it would be useful to study the remodeling of an arterio-venous network. Getting access to a realistic initial network is likely to pose a hard problem in particular if it must be artificially created. Further aspects to assess are interstitial fluid transport and O_2 release with associated intravascular O_2 decrease. Finally, vessel collapse and regression dominate the network remodelling process of the vasculature in the tumor center. In addition to anti-angiogenic factors solid stress is assumed to play a pivotal role in these processes. Therefore it would be highly desirable to incorporate an appropriate description of the dynamic evolution of solid stress in the tumor and its surrounding tissue to go beyond the phenomenological treatment of vessel collapse that we used in the model that we have presented in this work.

References

Alarcon, T., Byrne, H.M., Maini, P.K., 2003. A cellular automaton model for tumour growth in inhomogeneous environment. J. Theor. Biol. 225, 257–274.

Anderson, A.R.A., Chaplain, M.A.J., 1998. Continuous and discrete mathematical models of tumor-induced angiogenesis. Bull. Math. Biol. 60, 857–900.

Baish, J.W., Jain, R.K., 2000. Fractals and cancer. Persp. Cancer Res. 60, 3683–3688.

Bartha, K., Rieger, H., 2006. Vascular network remodeling via vessel cooption, regression and growth in tumors. J. Theor. Biol. 241, 903–918.

Betteridge, R., Owen, M.R., Byrne, H.M., Alarcon, T., Maini, P.K., 2006. The impact of cell crowding and active cell movement on vascular tumour growth. Networks and Heterogeneous Media 1, 515–535.

Breward, C.J., Byrne, H.M., Lewis, C.E., 2003. A multiphase model describing vascular tumour growth. Bull. Math. Biol. 65, 609–640.

Briggs, W.L., Henson, V.E., McCormick, S.F., 2001. A Multigrid Tutorial. The Society for Industrial and Applied Mathematics (SIAM).

Bru, A., Albertos, S., Subiza, J.L., Lopez, J., Garcia-Asenjo, Bru, I., 2003. The universal dynamics of tumor growth. Biophys. J. 85, 2948–2961.

Byrne, H.M., Chaplain, M.A.J., 1995. Mathematical models for tumour angiogenesis: numerical simulations and nonlinear wave solutions. Bull. Math. Biol. 57, 461–486.

Byrne, H.M., Alarcon, T., Owen, M.R., Webb, S.D., Maini, P.K., 2006. Modelling aspects of cancer dynamics: a review. Philos. Trans. R. Soc. London Ser. A 364, 1563–1578.

Carmeliet, P., Jain, R.K., 2000. Angiogenesis in cancer and other diseases. Nature 407, 249–257.

Chaplain, M.A.J., McDougall, S.R., Anderson, A.R.A., 2006. Mathematical modelling of tumor-induced angiogenesis. Annu. Rev. Biomed. Eng. 8, 233–257.

Chung, H.-W., Chung, H.-J., 2001a. Fractals and cancer. Cancer Res. 60, 3683–3688 (Correspondence re: J.W. Baish, R.K. Jain).

Chung, H.-W., Chung, H.-J., 2001b. Fractals and cancer. Cancer Res. 61, 8347–8351 (Correspondence re: J.W. Baish, R.K. Jain).

Cormen, T.H., Leiserson, C.E., Rivest, R.L., Stein, C., 1990. Introductions to Algorithms. Chapter 23.4: Topological Sort. MIT Press/ McGraw-Hill, Cambridge, MA/New York, pp. 485–488.

Davis, T., 2004. Algorithm 832: UMFPACK, an unsymmetric-pattern multifrontal method. ACM Transactions on Mathematical Software 30, 196–199.

Dimmeler, S., Zeiher, A.M., 2000. Endothelial cell apoptosis in angiogenesis and vessel regression. Circ. Res. 87, 434–439.

Döme, B., Paku, S., Somlai, B., Tímár, J., 2002. Vascularization of cutaneous melanoma involves vessel co-option and has clinical significance. J. Pathol. 197, 355–362.

Döme, B., Hendrix, M.J.C., Paku, S., Tóvári, J., Tímár, J., 2007. Alternative vascularization mechanisms in cancer pathology and therapeutic implications. J. Pathol. 170, 1–15.

Drasdo, D., Höhme, S., 2005. A single-cell-based model of tumor growth in vitro: monolayers and spheroids. Phys. Biol. 2, 133–147.

Eden, M., 1961. In: Neyman, J. (Ed.), Proceedings of the Fourth Berkley Symposium on Mathematics and Probability. University of California Press, Berkley, pp. 223–240.

Erber, R., Eichelsbacher, U., Powajbo, V., Korn, T., Djonov, V., Lin, J., Hammes, H.-P., Grobholz, R., Ullrich, A., Vajkoczy, P., 2006. EphB4 controls blood vascular morphogenesis during postnatal angiogenesis. EMBO Journal, 25 628–41.

Fung, Y.C., 1993. Biomechanics. Springer, New York.

Gazit, Y., Berk, D.A., Michael Leunig, L.T.B., Jain, R.K., 1995. Scale-invariant behavior and vascular network formation in normal and tumor tissue. Phys. Rev. Lett. 75, 2428–2431.

Gerhardt, H., Golding, M., Fruttinger, M., Ruhrberg, C., Lundkvist, A., Abramsson, A., Jeltsch, M., Mitchell, C., Alitalo, K., Shima, D., Betsholz, C., 2003. VEGF guides angiogenic sprouting utilizing endothelial tip cell filopodia. J. Cell Biol. 161, 1163–1177.

Gimbrone, M.A., Cotran, R.S., Leapman, S.B., Folkman, J., 1974. Tumor growth and neo-vascularization: an experiment model using the rabbit cornea. J. Nat. Cancer Inst. 52, 413–427.

Glassner, A.S. (Ed.), 1994. Graphics Gems I (Chapter II.8). Digital Line Drawing. Academic Press, New York.

Gödde, R., Kurz, H., 2001. Structural and biophysical simulation of angiogenesis and vascular remodeling. Dev. Dyn. 220, 387–401.

Hassid, Y., Furman-Haran, E., Margalit, R., Eilam, R., Degani, H., 2006. Noninvasive magnetic resonance imaging of transport and interstitial fluid pressure in ectopic human lung tumors. Cancer Res. 66, 4159–4166.

Holash, J., Maisonpierre, P.C., Compton, D., Boland, P., Alexander, C.R., Zagzag, D., Yancopoulos, G.D., Wiegand, S.J., 1999a. Vessel cooption, regression, and growth in tumors mediated by angiopoietins and VEGF. Science 284, 1994–1998.

Holash, J., Wiegand, S., Yancopoulos, G., 1999b. New model of tumor angiogenesis: dynamic balance between vessel regression and growth mediated by angiopoietins and VEGF. Oncogene 18, 5356–5362.

Iyer, N.V., Kotch, L.E., Agani, F., Leung, S.W., Laughner, E., Wenger, R.H., Gassmann, M., Gearhart, J.D., Lawler, A.M., Yu, A., Semeza, G.L., 1998. Cellular and developmental control of O-2 homeostasis by hypoxia-inducible factor 1 alpha. Genes Dev. 12, 149–162.

Ji, J.W., Tsoukias, N.M., Goldman, D., Popel, A.S., 2006. A computational model of oxygen transport in skeletal muscle for sprouting and splitting modes of angiogenesis. J. Theor. Biol. 241, 94–108.

Lee, D.-S., Bartha, K., Rieger, H., 2006. Flow correlated percolation during vascular remodelling in growing tumors. Phys. Rev. Lett. 96, 058104-1–058104-4.

Levine, H.A., Sleeman, B.D., Nilsen-Hamiltion, M., 2001. Mathematical modeling of the onset of capillary formation initiating angiogenesis. J. Math. Biol. 42, 195–238.

Lowengrub, J.S., Frieboes, H.B., Wise, S., Zheng, X., Macklin, P., Bearer, E., Cristini, V., 2007. Computer simulation of glioma growth and morphology. NeuroImage 37, 59–70.

Mantzaris, N.V., Webb, S., Othmer, H.G., 2004. Mathematical modeling of tumor-induced angiogenesis. J. Math. Biol. 49, 111–187.

McDougall, S.R., Anderson, A.R.A., Chaplain, M.A.J., Sherratt, J.A., 2002. Mathematical modelling of flow through vascular networks: implications for tumor-induced angiogenesis and chemotherapy strategies. Bull. Math. Biol. 64, 673–702.

McDougall, S.R., Anderson, A.R.A., Chaplain, M.A.J., 2006. Mathematical modelling of dynamic adaptive tumour-induced angiogenesis: clinical implications and therapeutic targeting strategies. J. Theor. Biol. 241, 564–589.

Minchinton, A.I., Tannock, I.F., 2006. Drug penetration in solid tumours. Nat. Rev. Cancer 6, 583–592.

Nehls, V., Herrmann, R., Hühnken, M., 1998. Guided migration as a novel mechanism of capillary network remodeling is regulated by fibroblast growth factor. Histochem. Cell Biol. 109, 319–329.

Paku, S., 1998. Current concepts of tumor-induced angiogenesis. Pathol. Oncol. Res. 4, 62–75.

Plank, M.J., Sleeman, B.D., 2003. A reinforced random walk model of tumour angiogenesis and anti-angiogenic strategies. Math. Med. Biol., 20135–20181.

Plank, M.J., Sleeman, B.D., 2004. Lattice and non-lattice models of tumour angiogenesis. Bull. Math. Biol. 66, 1785–1819.

Preziosi, L. (Ed.), 2003. Cancer modelling and simulation. In: Preziosi, L. (Ed.), Mathematical and Computational Biology, vol. 3. Chapman & Hall/CRC Press, London/Boca Raton.

Pries, A.R., Secomb, T.W., Gaehtgens, P., Gross, J.F., 1990. Blood flow in microvascular networks. Experiments and simulation. Circ. Res. 67, 826–834.

Pries, A.R., Secomb, T.W., Gessner, T., Sperandio, M.B., Gross, J.F., Gaehtgens, P., 1994. Resistance to blood flow in microvessels in vivo. Circ. Res. 75, 904–915.

Pries, A.R., Secomb, T.W., Gaehtgens, P., 1998. Structural adaptation and stability of microvascular networks: theory and simulations. Am. J. Physiol. Heart Circ. Physiol. 275, 349–360.

Sansone, B.C., Scalerandi, M., Condat, C.A., 2001. Emergence of taxis and synergy in angiogenesis. Phys. Rev. Lett. 87, 128102.

Secomb, T.W., Hsu, R., Park, E.Y.H., Dewhirst, M.W., 2004. Green's function methods for analysis of oxygen delivery to tissue by microvascular networks. A. Biomed. Eng. 32, 1519–1529.

Sun, S.Y., Wheeler, M.F., Obeyesekere, M., Patrick, C.W., 2005. A deterministic model of growth factor-induced angiogenesis. Bull. Math. Biol. 67, 313–337.

Tong, S., Yuan, F., 2001. Numerical simulations of angiogenesis in the cornea. Microvasc. Res. 61, 14–27.

Yu, J.L., Rak, J.W., Coomber, B., Hicklin, D.J., Kerbel, R.S., 2002. Effect of p53 status on tumor response to antiangiogenic therapy. Science 295, 1526–1528.

Zheng, X., Wise, S.M., Cristini, V., 2005. Nonlinear simulation of tumor necrosis, neo-vascularization and tissue invasion via an adaptive finite-element/level-set method. Bull. Math. Biol. 67, 211–259.